Towards sector-based attribution using intra-city variations in satellite-based emission ratios between CO_2 and CO

Dien Wu[1], Junjie Liu[2], Paul O. Wennberg[1,3], Paul I. Palmer[2,4], Robert R. Nelson[2], Matthäus Kiel[2], and Annmarie Eldering[2]

[1]Division of Geological and Planetary Sciences, California Institute of Technology, Pasadena, USA
[2]Jet Propulsion Laboratory, California Institute of Technology, Pasadena, USA
[3]Division of Engineering and Applied Science, California Institute of Technology, Pasadena, USA
[4]School of GeoSciences, University of Edinburgh, Edinburgh, UK

Correspondence: Dien Wu (dienwu@caltech.edu)

Abstract. Carbon dioxide (CO_2) and air pollutants such as carbon monoxide (CO) are co-emitted by many combustion sources. Previous efforts have combined satellite-based observations of multiple tracers to calculate their emission ratio (ER) for inferring combustion efficiency at regional to city scale. Very few studies have focused on burning efficiency at the sub-city scale or related it to emission sectors using space-based observations. Several factors are important for deriving spatially-resolved ERs from asynchronous satellite measurements including 1) variations in meteorological conditions induced by different overpass times, 2) differences in vertical sensitivity of the retrievals (i.e., averaging kernel profiles), and 3) interferences from the biosphere and biomass burning. In this study, we extended an established emission estimate approach to arrive at spatially-resolved ERs based on retrieved column-averaged CO_2 (XCO_2) from the Snapshot Area Mapping (SAM) mode of the Orbiting Carbon Observatory-3 (OCO-3) and column-averaged CO from the TROPOspheric Monitoring Instrument (TROPOMI). To evaluate the influence of the confounding factors listed above and further explain the intra-urban variations in ERs, we leveraged a Lagrangian atmospheric transport model and an urban land cover classification dataset and reported ER_{CO} from the sounding-level to the overpass- and city- levels. We found that the difference in the overpass times and averaging kernels between OCO and TROPOMI strongly affect the estimated spatially-resolved ER_{CO}. Specifically, a time difference of > 3 hours typically led to dramatic changes in the wind direction and shape of urban plumes and thereby making the calculation of accurate sounding-specific ER_{CO} difficult. After removing those cases from consideration and applying a simple plume shift method when necessary, we discovered significant contrasts in combustion efficiencies between 1) two megacities versus two industry-oriented cities and 2) different regions within a city, based on six to seven nearly-coincident overpasses per city. Results suggest that the combustion efficiency for heavy industry in Los Angeles is slightly lower than its overall city-wide value (< 10 ppb-CO / ppm-CO_2). In contrast, ERs related to the heavy industry in Shanghai are found to be much higher than Shanghai's city-mean and more aligned with city-means of the two industry-oriented Chinese cities (approaching 20 ppb-CO / ppm-CO_2). Although investigations based on a larger number of satellite overpasses are needed, our first analysis provides guidance for estimating intra-city gradients in combustion efficiency from future missions, such as those that will map column CO_2 and CO concentration simultaneously with high spatiotemporal resolutions.

1 Introduction

Home to more than half of the total global population, urban areas have been expanding, especially for Asia and Africa with an urbanization rate of 1.3% and 1.1% yr^{-1} between 2015 and 2020 (World Urbanization Prospects 2018). Urban regions are also responsible for a significant amount of anthropogenic emissions of greenhouse gases and air pollutants into the atmosphere including carbon dioxide (CO_2), methane, carbon monoxide (CO), and nitrogen oxides (Duncan et al., 2016; Lin et al., 2018; Super et al., 2017; Plant et al., 2019). To monitor the abundance of a number of atmospheric species in a globally-consistent manner, satellite observations have become indispensable in past years (Yokota et al., 2009; Crisp et al., 2012; Veefkind et al., 2012). For example, carbon-monitoring satellites such as the Orbiting Carbon Observatory-2 (OCO-2, Crisp et al., 2012) have made the quantification of city-scale CO_2 emissions and emission trends possible (e.g., Hedelius et al., 2018; Ye et al., 2020; Wu et al., 2020; Shekhar et al., 2020; Lei et al., 2021). Quantifying the spatial gradient of atmospheric concentrations and relating the gradient to emissions within the city domain becomes the next critical yet challenging task. Understanding such spatial heterogeneity in emissions and the environmental consequences can support better decisions in urban planning and pinpointing hotspots for emission mitigation.

To reduce emissions of greenhouse gases and air pollutants, targeting the efficiency during combustion activities is the key. Such efficiency is linked to the underlying combustion processes and conditions (e.g., oxygen-to-fuel ratio and temperature). For example, the amount of CO_2 emitted from coal-fired power plants varies with thermal and pressure conditions, the type of fuel consumed, the technology deployed, and the service duration of power plants (Yuan and Smith, 2011). Modern power generation with distinct scrubbing technology are often regarded as "clean" emitters leading to minimal CO and NO_x enhancements (Lindenmaier et al., 2014). The commonly-used approach in estimating combustion efficiency is to combine atmospheric observations of multiple trace gases. Benefit from the cancellation of the errors in describing the atmospheric transport that carries tracers to the measurement site, the ratio of the total or excess measured concentrations (above a defined background value) between tracers are reported (Silva and Arellano, 2017; Reuter et al., 2019; Park et al., 2021). A few notable studies further utilized their derived emission ratios (ERs) from ground or airborne measurements to infer sector-specific emission signals (Wennberg et al., 2012; Lindenmaier et al., 2014; Nathan et al., 2018; Tang et al., 2020).

CO and NO_x often serve as tracers for anthropogenic CO_2 due to their overlapping sources of combustion (e.g., Palmer et al., 2006; Wunch et al., 2009; Hedelius et al., 2018). Analyzing remotely-sensed NO_x plumes with relatively short lifetime can help identify local fossil fuel CO_2 ($FFCO_2$) sources that would otherwise be difficult (Reuter et al., 2019; Fujinawa et al., 2021). While at the same time, such reactivity raises the requirement of accurately accounting for chemical transformation and complicates the interpretation of emission signals or ERs from NO_x observations (Lama et al., 2020; Hakkarainen et al., 2021). CO with a much longer lifetime, on the other hand, is much easier to interpret and more likely to be found during incomplete combustion. The emission ratio of CO to CO_2 (ER_{CO}) is usually estimated from sparse ground-based measurements within a city (Bares et al., 2018; Chandra et al., 2016; Lindenmaier et al., 2014) and from satellites at the city scale (Park et al., 2021; Silva and Arellano, 2017). Sector-specific activities and ER_{CO} such as from the traffic sector have been diagnosed by limited, but valuable, tunnel studies (Ammoura et al., 2014; Bradley et al., 2000; Popa et al., 2014).

We performed a literature search on ER_{CO} derived from observations (**Appendix A**) and summarize their values in **Fig. 1**.
Combustion efficiency fluctuates 1) over time (e.g., Turnbull et al., 2011b), likely explained by technological improvements and
60 2) between sub-sectors, e.g., gasoline vs. diesel vehicles or moving vs. congestion traffic (Westerdahl et al., 2009; Popa et al.,
2014). Despite differences in measurement platforms and analyzing approaches, the observed urban-integrated ER_{CO} values,
especially for those in Europe and the United States, are well constrained within the range of 4 to 15 ppb ppm^{-1}(**Fig. 1b**).
ER_{CO} for biomass burning and shipping sectors are estimated based on fuel-specific emission factors, i.e., ER_{CO} (= EF_{CO} /
EF_{CO_2}) with proper unit conversions, where EF_X indicates the emission of gas X per kg of fuel burned.
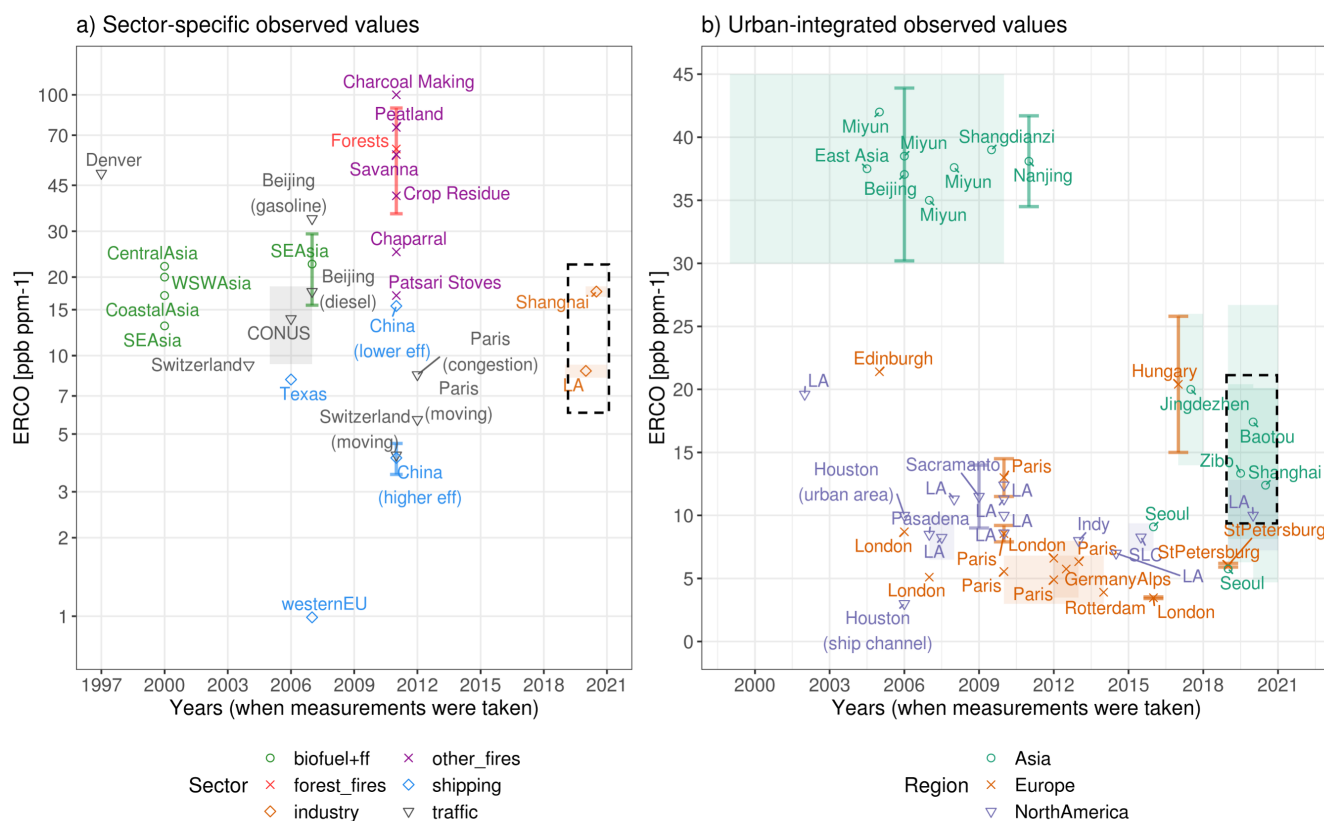

Figure 1. ER_{CO} [ppb ppm^{-1}] associated with specific processes (a) and ER_{CO} integrated over the entire city/region (b) summarized from previous studies.
X-axis indicates the time these estimates were made except for Akagi et al. (2011). 2011 was simply chosen for x-axis since the paper was published in 2011.
The error bars represent the uncertainties in estimated ERs and transparent rectangle indicates the range of ERs over multiple years. Paper citations are omitted
from the figure and included in **Appendix A**. ERs related to biomass burning and the shipping sectors are derived using emission factors of CO and CO_2. The
range of the overpass-specific ER_{CO} estimates for Shanghai, LA, Baotou, and Zibo derived from this work are also added to the figure (dashed black box).

65   The variability in observation-derived ERs among different combustion processes and sectors (**Fig. 1a**) hinders the gener-
alization and representation of gridded ERs. Many bottom-up emission inventories simulate $FFCO_2$ emissions using activity
data for spatially allocating sector-based EFs (Gurney et al., 2019; Solazzo et al., 2021). One notable example is Hestia, a

high-resolution inventory for the US, which estimates CO_2 emissions of non-point sources based upon CO emissions from the National Emission Inventory, EF_{CO}, and EF_{CO_2} and carefully evaluates their adopted EFs (Gurney et al., 2019). However, con-
70 structing inventories for the entire globe is data-demanding and challenging because accurate bottom-up estimates require activity data and EF_X that vary with combustion conditions (e.g., temperature, fuel load, oxygen level) and are generally not well known, especially over data-scarce regions. To our knowledge, only a few global inventories, such as the Emissions Database for Global Atmospheric Research (EDGAR, Solazzo et al., 2021), offer global anthropogenic CO and CO_2 emissions. Considering the challenge in approximating ERs, the knowledge derived from observations may 1) complement inventory-based ERs
75 (e.g., CO:NO_x ratio in Lama et al., 2020) and 2) facilitate the emission constraint for a desired species, usually with relatively large uncertainties (Wunch et al., 2009; Palmer et al., 2006; Wang et al., 2009; Brioude et al., 2012; Nathan et al., 2018). Such prior success motivates us to derive ERs from satellite observations of multiple tracers.

Most previous studies have focused on quantifying an integrated ER for the whole city or region. As a step forward, we zoom into an urban area and leverage spatially-resolved satellite observations. Intra-city variations in the satellite-based concentration
80 of a specific air pollutant like NO_x have been examined and linked to societal inequality such as of income and educational attainment (Demetillo et al., 2021; Kerr et al., 2021). Yet, no one has attempted to study the intra-urban gradient in combustion efficiency from space and connect such gradient to a specific combustion process. This is now possible by virtue of the Orbiting Carbon Observatory-3 (OCO-3) mounted on the International Space Station (ISS) that can sample a city-landscape during its Snapshot Area Mapping (SAM) mode (Eldering et al., 2019; Taylor et al., 2020; Kiel et al., 2021). In this effort to arrive at
85 spatially-varying ERs from sensors with asynchronous orbits, we must account for several factors that have not been thoroughly investigated. These include 1) variations in meteorological conditions during different overpass times, 2) discrepancies in vertical sensitivity of the retrievals (i.e., averaging kernel or AK profiles), and 3) interference from non-anthropogenic sources and sinks.

Motivated by the gaps in prior literature, we conducted an analysis to explore the spatial distribution of ER_{CO} within
90 four urban areas mainly using XCO_2 observations from OCO-3 and XCO observations from the TROPOspheric Monitoring Instrument on board the Sentinel-5 Precursor (TROPOMI, Veefkind et al., 2012). To avoid relying on prior sectoral information on ER_{CO} from emission inventories, we adopt urban land cover data from the high-resolution World Urban Database and Access Portal Tools (WUDAPT, Ching et al., 2018). WUDAPT offers the so-called Local Climate Zone (LCZ) that takes into account building structures/spacing and vegetation coverage (Stewart and Oke, 2012), which can shed light on localized
95 infrastructure within the city.

Our work seeks to answer the following two questions.

1. Is it possible to quantify accurate spatially-resolved ER_{CO} from asynchronous satellite measurements?

2. Can the combustion efficiency for a given sector be determined without using prior emission inventories?

In Section 2, we describe the satellite data and methodology for obtaining emissions, ER_{CO}, and associated uncertainties. In
100 Section 3, we present the results on intra-city variations in ER_{CO} (including ER_{CO} tied to heavy industry areas in a megacity) and its sensitivity to several interference factors. In Section 4, we discuss the implication and limitation of this analysis.

2 Data and methodology

We targeted two types of cities: 1) industry- and energy- oriented cities (Baotou, China and Zibo, China), and 2) megacities with more diverse emission sectors (Shanghai, China and Los Angeles, US). The four cities are selected considering the amount

105 and quality of XCO_2 data from OCO-3 SAMs and TROPOMI XCO data. The two industry- and energy- oriented cities in China are selected given their considerable amount of metal production plants for aluminum or iron and steel (Global Energy Infrastructure Emission Database, GID; Wang et al., 2019) and surrounded coal-fired power plants (Global Energy Monitor, GEM; and the Global Power Plant Dataset; World Resources Institute, 2018) that support the nearby industries.

Our goal is to calculate ER_{CO} from every satellite sounding within an urban plume that is the spatial extent affected by

110 urban emissions (**Sect. 2.2**). Sounding-dependent ER_{CO} are calculated as ratios of CO emissions over CO_2 emissions (**Eq. 3**) that estimated from the satellite-derived FF enhancements and further refined with a "scaling factor" in **Eq. 1**. This scaling factor is obtained from an atmospheric transport model (**Sect. 2.2.1**), which accounts for several mismatches between OCO-2/3 and TROPOMI (**Sect. 2.1**). Determination of FF enhancements requires estimate of the background values (**Sect. 2.2.2**) and "second-order" correction terms for biogenic and pyrogenic sources (see explanations in **Sect. 2.2.3**). The sounding-specific

115 ERs and their uncertainties (**Sect. 2.2.4**) are aggregated to yield ER per overpass and per city. After determining the intra-city variations in ER, we illustrate how much ERs associated with heavy industry in Los Angeles and Shanghai can be extracted with the assistance of the urban land cover classification dataset (WUDAPT, **Sect. 2.3**).

2.1 Satellite observations and data pre-processing

We screened available data for overpass coincidences between OCO-3 SAM XCO_2 and TROPOMI XCO observations with

120 relatively small differences in overpass times. Considering the limited number of the coincidences between sensors, two non-SAM overpasses from OCO-3 and one OCO-2 overpass are added to the analysis. In the end, six to seven OCO-TROPOMI coincidences with higher data quality from Oct 2019 to June 2021 were integrated into the final result for each city. Only two of the total 25 overpasses (both in June 2021) fall within the north hemispheric summer months between June and August.

2.1.1 OCO-2/3 XCO_2

125 The column-averaged dry-air mole fraction of CO_2 (XCO_2) is retrieved from reflected sunlight over two CO_2 bands centered on 1.6 and 2.0 μm and the oxygen-A band for obtaining surface pressure obtained by OCO-3 (Eldering et al., 2019; Taylor et al., 2020). In addition to the standard Nadir, Glint, and Target modes, OCO-3 performs SAMs that collect several adjacent swaths of XCO_2 observations over a spatial area of approximately 80 km by 80 km, e.g., four individual swaths in an overpass over LA on Feb 24, 2020 (**Fig. 2a**). Similar to OCO-2, each swath is comprised of eight spatial footprints/soundings and each

130 sounding has an area of $\sim$1.6$\times$2.2 km^2 at nadir (**Fig. 2a**). Our analysis only used screened OCO-3 B10r data (Eldering, 2021) with an XCO_2 quality flag of zero (QF = 0). It is worth highlighting that the B10r product is superior to the Early version for OCO-3 (Taylor et al., 2020) including improved geolocation, advanced radiometric calibration, improved quality filters and

customized post processing bias correction. Because OCO-3 is mounted on the ISS that is in a precessing orbit, its overpass time varies, for example, from 07 to 15 local time for the overpasses we examined.

2.1.2 TROPOMI XCO

The column density of CO molecules [mole cm^{-2}] is retrieved via the measured radiation from the shortwave infrared wavebands on TROPOMI, centered at $\sim$2.3 μm (Veefkind et al., 2012). We only selected data with quality assurance $\geq$ 0.5 recommended by the TROPOMI readme document (Landgraf et al., 2020) and converted the column density to the total column-averaged dry-air mole fraction of CO [ppb] using dry-air column density [mole cm^{-2}] estimated from retrieved surface pressure and total column water vapor. TROPOMI CO is retrieved at a larger pixel area of $\sim$7$\times$7 km^2 at Nadir and reduced to 5.5$\times$7 km^2 after Oct 6, 2019 (**Fig. 2c**). The overpass time of TROPOMI is $\sim$13:30 local time of equatorial overpass for nadir measurements with a time span of 1–2 hours for soundings on the edge of its wide swath (i.e., $\sim$2600 km).

2.1.3 Differences between two sensors/species

Four mismatches between OCO-3 XCO$_2$ and TROPOMI XCO pose challenges in extracting FF enhancements and ER$_{CO}$ from atmospheric observations, which we attempt to account for and assess:

1. *Satellite pixel area:* We searched for OCO-2/3 soundings falling within each TROPOMI polygon and averaged the corresponding XCO$_2$ enhancements to the TROPOMI scale (**Fig. 2a vs. b**). For simplicity, we used the centered lat/lon coordinate of an OCO-3 sounding to determine its corresponding TROPOMI polygon. Retrieval uncertainties and observation noise (defined as the XCO$_2$ variability within each TROPOMI polygon) are estimated at the TROPOMI pixel scale and propagated as part of the total observed uncertainty (**Sect. 2.2.4**).

2. *Averaging kernel profile:* Within the planetary boundary layer where most emissions occur, TROPOMI XCO retrieval is affected by cloud height/fractions, which yields lower-than-unity AK (**Supplementary Fig. S1**). OCO-2/3 XCO$_2$ under cloudy conditions are typically omitted from Lite files and when QF = 0 is applied; thus, its AK normally approaches one near the surface for cloud-free scenes. The mismatch in AKs between sensors must be accounted for as it can affect the interpretation of ERs. In this work, we accounted for AK within an atmospheric transport model (**Sect. 2.2.1**).

3. *Overpass time and upwind meteorological condition:* As result of the sometimes large time difference, meteorological conditions including the wind direction and speed can change significantly, leading to changes in urban plume shapes detected by the two sensors as they pass by. We dealt with changes in wind speed and wind direction separately. The former is resolved by the "scaling factor" generated from the atmospheric transport model and the latter undergoes manual evaluations (**Sect. 3.1**).

4. *Non-fossil fuel sources/sinks:* The influence from the biosphere and biomass burning may affect the calculation of ER$_{CO}$. Given our definition of background regions, the contrast in non-FF anomalies between the urban and background region may interfere the calculation of FF enhancements and ER$_{CO}$ (more explanations in **Sect. 2.2.3**).
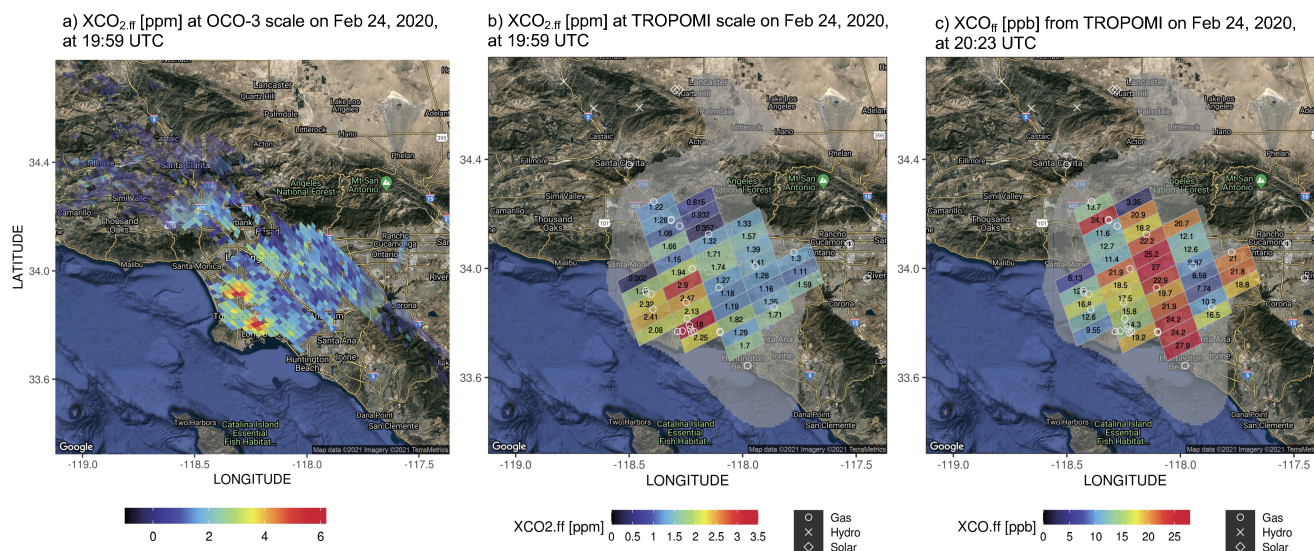
Figure 2. FF XCO_2 enhancements at the native OCO-3 soundings (a, ppm) and aggregated to the TROPOMI scale (b, ppm), and XCO enhancements (c, ppb) over Los Angeles on Feb 24, 2020. Power stations with different primary fuel types are displayed in different white symbols based on the Global Power Plant Dataset (World Resources Institute, 2018). The X-STILT column footprint [ppm / (μmol m^{-2} s^{-1})] from all soundings are drawn in light grey (see explanations for column footprint in **Sect. 2.2.1**). The underlying hybrid maps were created using ggmap library in R that adopted the Google Maps (copyright: Map data ©2021 Imagery ©2021 TerraMetrics).

2.2 Estimates of E_{gas}, ER_{CO} and uncertainties

165 Previous studies (Mitchell et al., 2018; Wu et al., 2020; Lin et al., 2021) proposed an approach to calculate the overall CO_2 or CH_4 fluxes using atmospheric measurements and atmospheric transport model without prior information from emission inventories. Here we briefly describe this approach to obtain the overall emission of either CO_2 (**Eq. 1**) or CO (**Eq. 2**) for each sounding S, modified from Wu et al. (2020):

$$\langle E_{\mathrm{CO_2,s}} \rangle = \frac{X_{\mathrm{ffCO_2,s}}}{\langle XF_{\mathrm{CO_2,s}} \rangle} = \frac{X_{\mathrm{obsCO_2,s}} - X_{\mathrm{bgCO_2}} - \delta X_{\mathrm{bioCO_2,s}} - \delta X_{\mathrm{bbCO_2,s}}}{\iint XF_{\mathrm{CO_2,s}}(x,y)\,dx\,dy}. \tag{1}$$

170 $$\langle E_{\mathrm{CO,s}} \rangle = \frac{X_{\mathrm{ffCO,s}}}{\langle XF_{\mathrm{CO,s}} \rangle} = \frac{X_{\mathrm{obsCO,s}} - X_{\mathrm{bgCO}} - \delta X_{\mathrm{bbCO,s}}}{\iint XF_{\mathrm{CO,s}}(x,y)\,dx\,dy}. \tag{2}$$

All X terms in the numerator contribute to FF enhancements (X_{ff}, **Fig. 2**). In theory, X_{ff} at a downwind satellite sounding S is the sum of its corresponding FF sources over its corresponding source region (x, y). To describe and attribute this source region to each satellite sounding, we adopted the column version of the Stochastic Time-Inverted Lagrangian Transport (X-STILT) model (Lin et al., 2003; Fasoli et al., 2018; Wu et al., 2018). Using X-STILT, we can obtain a "scaling factor" $\langle XF_{\mathrm{gas}} \rangle$

175 that accounts for sounding-specific AK profile and meteorology (**Sect. 2.2.1**).

Within the calculation of FF enhancements of either XCO_2 or XCO, X_{bg} represents the background values calculated from observations uncontaminated by the urban plume, which are normally constant for a group of observations (i.e., not sounding-specific, **Sect. 2.2.2**). The air parcels arriving at the sounding in the city center can have different origins and pathways from the air parcels tied to a rural sounding. These two soundings may be influenced differently by biospheric fluxes and biomass burning emisions. Hence, two background correction δ-terms are attached to correct for the urban-background gradient in column anomalies from the net ecosystem exchange (NEE) and biomass burning (**Sect. 2.2.3 and Eq. 4**).

Similar to X_{ff}, the resultant flux $\langle E_{gas} \rangle$ with unit of μmol m^{-2} s^{-1} is tied to each sounding. These fluxes represent the total emissions in the source region with respect to a given TROPOMI sounding and should not be confused with the direct emission at that sounding location. The ER_{CO} for a given sounding S is then derived from **Eqs. 1 and 2** as follows:

$$ER_{CO} = \frac{\langle E_{CO} \rangle}{\langle E_{CO_2} \rangle} = \frac{X_{ffCO}}{X_{ffCO_2}} \frac{\langle XF_{CO_2} \rangle}{\langle XF_{CO} \rangle} = \frac{X_{ffCO}}{X_{ffCO_2}} \gamma_{foot}. \tag{3}$$

$\frac{X_{ffCO}}{X_{ffCO_2}}$ is the enhancement ratio and γ_{foot} informs how enhancement ratios without accounting for AKs and meteorology differ from emission ratios. We simply use ppb-CO/ppm-CO$_2$ for units of ER_{CO} (same as mmol-CO/mol-CO$_2$).

2.2.1 The X-STILT model

The X-STILT model is adopted for three purposes: to 1) provide the scaling factor $\langle XF_{gas} \rangle$ that resolves the influences from differences in AK and wind fields between sensors; 2) identify the overpass-specific urban plume for background determination (**Sect. 2.2.2**), and to; 3) estimate the sounding-level biogenic and pyrogenic contributions to the background (**Sect. 2.2.3**).

STILT releases an ensemble of air parcels from target observations (known as the STILT "receptor") and tracks the movement of those air parcels backward in time. The source region corresponding for each sounding is informed by the "source-receptor relation" or the STILT "footprint" (Lin et al., 2003; Fasoli et al., 2018). The STILT footprint [ppm / (μmol m^{-2} s^{-1})] describes the change in atmospheric concentration [ppm] at a downwind location due to possible upwind sources/sinks [μmol m^{-2} s^{-1}]. The magnitude of STILT footprints tend to be higher close to the target observations or under steadier wind condition, as air parcels within the boundary layer can interact more with fluxes from the surface.

To accommodate the use of satellite-based column data, X-STILT incorporates the retrieval-specific AK and pressure weighting (PW) profiles in the footprint calculation (Wu et al., 2018), such that the influence of air parcels originating from various altitudes of an atmospheric column are weighted by sounding- and sensor- specific AK profile (**Supplementary Fig. S2**). The "column footprint", XF_{gas}, becomes the sensitivity of the total column concentration to upwind fluxes. Because AK profile is specific to the retrieval, XF_{gas} for TROPOMI XCO differs from that for OCO-2/3 XCO_2 even for concurrent observations (**Eqs. 2, 1**). Because the air flow arriving at each satellite observation is unique, the magnitude and spatial distribution of column footprints vary from one sounding to another (**Supplementary Fig. S3**). If taking an average of these sounding-dependent column footprints, as shown in **Supplementary Fig. S3**, we can identify the source region for all soundings in a SAM as indicated by the light gray area in **Fig. 2b,c**. In this work, we only traced air parcels for 12 hours backward in time for calculating column footprints, which is sufficient to capture the near-field influence from the target city.

Atmospheric
Chemistry
and Physics
Discussions

Open Access

EGU

In summary, the spatial summation of column footprints $\langle XF_{\mathrm{gas}} \rangle$ is regarded as a scaling factor in addressing the sensor-specific meteorological condition and AK profile. The deviation of the term γ_{foot} in **Eq. 3** from 1 reveals the difference between

210   a simple concentration enhancement ratio and a more robust, model-corrected emission ratio.

2.2.2 Background definition X_{bg}

Defining accurate background levels to extract urban FF enhancements has always been a challenge in top-down analysis, especially when dealing with column measurements with small signal-to-noise ratio. Wu et al. (2018) compared several approaches to determine the localized XCO_2 background for extracting urban signals from OCO-2, including approaches that 1)

215   solely use satellite observations with statistics like percentile or median; 2) solely use atmospheric transport models (e.g., curtain method and global concentration fields); and 3) combines observations and model. The latter two methods do not involve prior information on emissions. Here, we expand the third approach to arrive at swath-dependent XCO and XCO_2 background values. The broader spatial coverage and multiple swaths of stretching out of the city domain of OCO-3 SAMs improve the determination of the background terms by introducing spatial variations in the background. Accurately describing the spatial

220   gradients in background XCO_2 have been emphasized previously (Ye et al., 2020; Schuh et al., 2021).

The process of background determination used in this work involves a first step of identifying the urban plume and differentiating soundings within or outside of the plume. Here we used the forward mode of STILT with the inclusion of wind uncertainty to atmospheric dispersion. Specifically, 1000 air parcels were released continuously from a rectangle representing the urban extent (dashed black box in **Fig. 3**) every 30 minutes starting from 10 hours ahead of the overpass time. All air

225   parcels are allowed to travel forward in time for 12 hours from their initial release time. A random wind component typifying model-data wind errors is added to the parcel dispersion (Lin and Gerbig, 2005). We subset the air parcels during the overpass time and applied a 2-dimensional kernel density estimate (KDE) based on the parcels' spatial distribution (blue to purple contours in **Fig. 3**). KDE is carried out using the kde2d function provided by the MASS library in R (Venables and Ripley, 2002). These normalized KDE contours then denote the likelihood and shape of an urban plume when the satellite scans through.

230   The extent of the urban plume is finalized using a normalized KDE contour of 0.15 (black curve in **Fig. 3**), which is proper to 1) include soundings with possible influence from the target city and 2) exclude observations elevated by another city (e.g., the red polygons centered at around 32°N and 120°E in **Fig. 3c**). This procedure is carried out separately for OCO-2/3 and TROPOMI to address differences in the urban plume at different overpass times (see **Sect. 3.1**). It worth stressing that only enhancements within the urban plume are selected to yield ER_{CO}.

235   Next, the background value is calculated as the median value of observed X_{gas} per swath over the background region. For example, the background region is the area to the east outside the urban plume since southeasterly wind dominates (**Fig. 3b,c**). Background values vary with swaths if an OCO-3 SAM is examined. We chose the median instead of the mean to minimize the impact of any "outliers" that may be from a second FF source (other than our target cities) in the background region. When analyzing data from OCO-2's narrow swath (**Fig. 3a**), the latitude range outside the plume serves as the background region and

240   can be sensitive to the modeled wind bias and number of valid soundings (Wu et al., 2018). Fortunately, modeled wind bias

is generally less of an issue when analyzing SAMs, because the broader coverage of valid SAM observations helps evaluate model-based urban plumes. Background uncertainties are estimated and propagated into the ER uncertainty (**Sect. 2.2.4**).
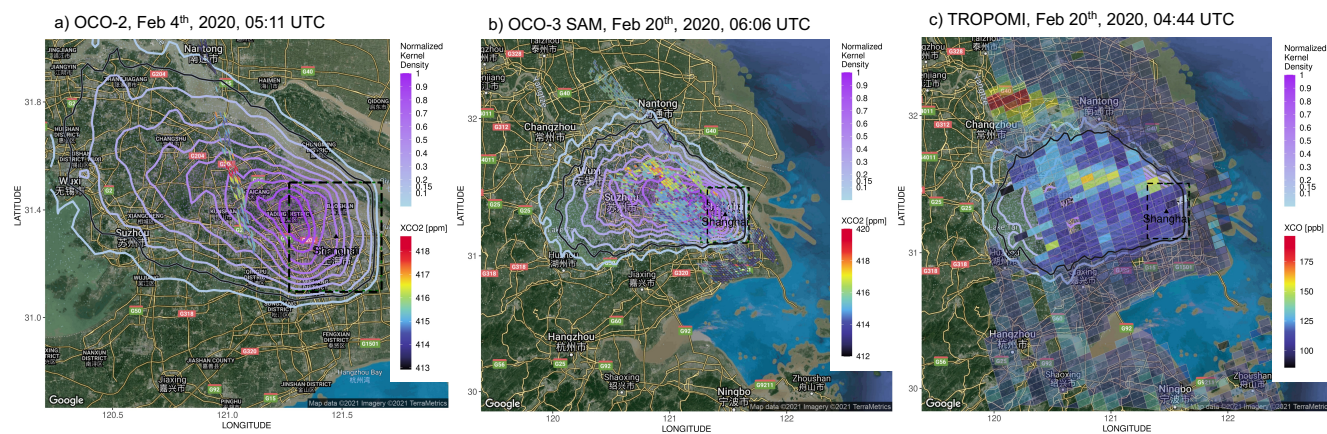

Figure 3. Demonstrations of background determination from OCO-2 XCO_2 on Feb 4, 2020 (a), OCO-3 SAM XCO_2 [ppm] and TROPOMI XCO [ppb] on Feb 20, 2020 (b, c) over Shanghai. The model-based urban plume (solid black curve) is determined by the normalized 2-D kernel density of the air parcels' distribution during the overpass time (blue-purple contours). On Feb 20, 2020, measurements to the east outside modeled plumes are identified as the "background measurements". The underlying maps were created using ggmap library in R that adopted the Google Maps (copyright: Map data ©2021 Imagery ©2021 TerraMetrics).

2.2.3 Background correction terms for non-FF sources/sinks

The swath-dependent background approach described above explicitly assumes equal contributions from non-FF sources and sinks for soundings in the background versus soundings in the urban plume. We further estimated urban-background gradients in X_{gas} resulting from biogenic and pyrogenic fluxes.

As initially proposed in Wu et al. (2021), rather than the absolute biogenic or pyrogenic concentration anomalies, it is the contrast in these anomalies between the background versus urban region that is required, given our background definition. Specifically, hourly column footprints from X-STILT are convolved respectively with hourly mean NEE from a biogenic model representation and the daily mean wildfire emissions from the Global Fire Assimilation System (GFAS, Kaiser et al., 2012) to estimate the absolute column anomalies X_{bio} and X_{bb} for every sounding. The Solar-Induced Fluorescence (SIF) for Modeling Urban biogenic Fluxes (SMUrF, Wu et al., 2021) model estimates gross primary production (GPP) from a Contiguous SIF product (CSIF trained based on OCO-2 SIF, Zhang et al., 2018) and respiration based on modeled SIF-based GPP, air and soil temperatures.

Next, the urban-background gradient in the anomalies are calculated as the difference between the sounding-specific anomalies and the average anomalies over the background region.

$$\delta X_{bioCO_2}(s) = X_{bioCO_2}(s) - \overline{X_{bioCO_2}(s_{bg})} \tag{4}$$

Atmospheric
Chemistry
and Physics
Discussions

Open Access

EGU

where s or s_{bg} represents all the soundings or selected soundings in the background region, respectively. Let us imagine a north hemispheric summer day at noon, when the urban core is normally associated with a weaker biospheric uptake than the surrounding rural region, biogenic signals $X_{bioCO_2}(s)$ for soundings in the city are less negative than the mean biogenic signal over the rural background $\overline{X_{bioCO_2}(s_{bg})}$. Hence, the urban-background biogenic gradient $\delta X_{bioCO_2}(s)$ is normally positive and should be subtracted from the observed column to yield the FF enhancement (**Eq. 1**). Modeled sounding-specific X_{bio}, the urban-background gradient δX_{bio}, and their impacts on ER_{CO} are discussed in **Sect. 3.1**.

Flux exchanges from the ocean and chemical transformation (e.g., CO sink via hydroxyl radical (OH) and source from oxidation of volatile organic compounds, VOCs) are not considered. The average lifetime of CO against OH lasts for a few weeks to several months depending on the season, much longer than the few-hour timescale we care about. Yet, CO can be generated from the oxidation of CH_4 and non-methane VOCs at various rates, which are discussed in **Sect. 4.3**.

2.2.4 ER_{CO} uncertainty

The uncertainty related to X_{gas} emissions should contain uncertainties from 1) atmospheric transport (i.e., column footprints), 2) the retrieval and measurement, 3) background, and 4) non-FF gradients. However, we neglect uncertainties from column footprints by assuming no systematic transport bias associated with the X-STILT simulations during OCO and TROPOMI overpass times. The urban-background gradient in non-FF fluxes remains very small compared to FF enhancements.

Observed uncertainty of XCO_2 are comprised of retrieval errors and measurement noise (or XCO_2 variability) as the standard deviation of XCO_2 observations within a TROPOMI polygon. Depending on the TROPOMI sounding size (nadir or not) and the amount of screened OCO-3 soundings, there could be 5 to 28 OCO-3 soundings per TROPOMI polygon. Background uncertainty contains the retrieval error and the measurement noise of observations over background regions. Retrieval errors associated with each OCO-3 sounding are aggregated to the TROPOMI spatial scale in a standard-deviation-of-mean manner. Hence, the fewer OCO-3 soundings in a given TROPOMI polygon, the larger the observed uncertainties will be, which accounts for the unequal OCO-3 sampling in a TROPOMI polygon.

2.3 Identifying ER_{CO} for heavy industry within a city

One key objective of our study is to explain the intra-city variability of ER_{CO} by exploring the sector-specific or sector-dominant burning activities. While certain combustion processes and sectors tend to have higher ERs than others, the sectoral-dependent ER are likely variable within and across cities. Moreover, the ERs determined from atmospheric observations comprise a mixed effect of different sectoral activities. Previous attempts include reducing the number of sectors and relying on prior knowledge of sector-specific ERs in a (joint) Bayesian inversion (Nathan et al., 2018; Brioude et al., 2012).

Here, we propose to identify ERs associated with heavy industry within a city. Instead of relying on prior emission inventories that can sometimes be erroneous regarding the magnitude and location of sectoral activities (see discussions in **Sect. 4.3**), we utilize a urban land cover classification dataset. The World Urban Database and Access Portal Tools (WUDAPT, **Fig. 4a, d**) project provides Local Climate Zone (LCZ) classifications at a grid spacing of 120 m (Ching et al., 2018). Example LCZ categories include street canyons (e.g., compact/open/lightweight, high-/mid-/low-rise), building spacing (e.g., sparsely built,
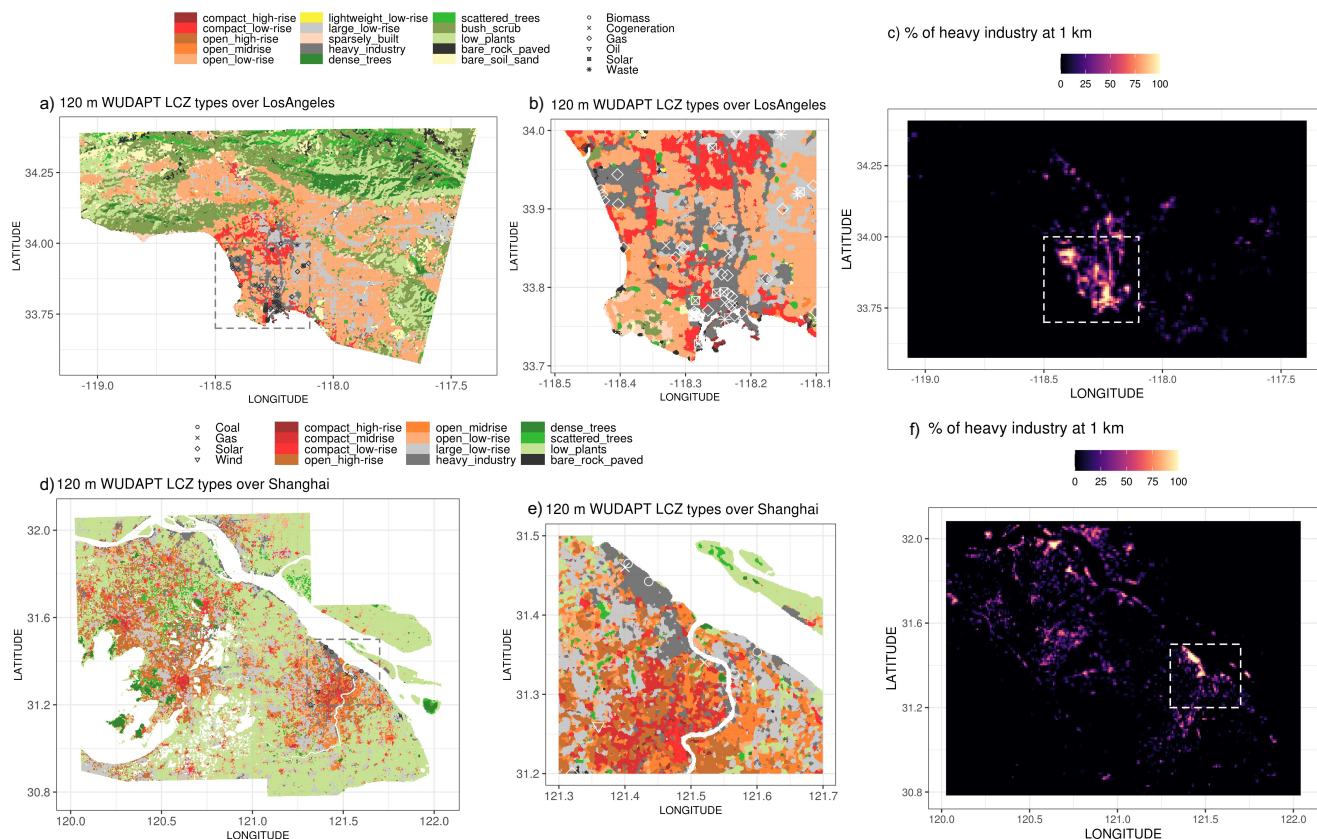
Figure 4. Map of Local Climate Zone (LCZ) from WUDAPT at a grid spacing of 120 m (a and d with zoomed-in images on b and e) and interpolated areal coverage of heavy industry [%] at 1 km around Shanghai and Los Angeles (c, f). LCZ classifications centered on Wuxi and Shanghai are combined. Power stations based on the Global Power Plant Dataset (World Resources Institute, 2018) are drawn on the map as different symbols. The lightgray and white dashed rectangles in the first and third columns indicate the zoomed-in region of the second column.

heavy industry), and tree spacing (e.g., e.g., dense/scattered trees, low plants, rocks, etc) (Stewart and Oke, 2012). Each LCZ is unique in its thermal, radiative, and metabolic properties. For instance, compact high-rise (LCZ 1) and heavy industry (LCZ 10) categories have the highest anthropogenic heat output of 50–300 W m^{-2} and > 300 W m^{-2}, respectively (Stewart and Oke, 2012). Heavy industry is defined as low-rise and mid-rise industrial structures (towers, tanks, stacks) and mostly paved

295 or hard-packed metal with steel and concrete construction materials with few or no trees (Ching et al., 2018), which differs from the industry-relevant sectors (e.g., from the Intergovernmental Panel on Climate Change). Some industries are also found within the WUDAPT-based heavy industry region (**Figure 4**). We clarify that we are not trying to tackle individual industrial processes, but treat some as an entity according to land cover data. Note that WUDAPT LCZ maps are only available for a limited number of cities across the globe including Shanghai and Los Angeles.

Atmospheric
Chemistry
and Physics
Discussions

Open Access
EGU

300   To relate ER_{CO} to heavy industry, the percentage of heavy industry is first interpolated at 1 km grid spacing from WUDAPT LZC maps (%, **Fig. 4c,f**). Those industry coverage are then convolved with the X-STILT column footprint (**Supplementary Fig. S3**) to quantify the industrial influence on each TROPOMI polygon $P_{ind}(x,y)$, which is defined as the column footprint-normalized industry fraction (**Supplementary Fig. S4**). For example, soundings in the city center farther away from the heavy industry are related to smaller influences. Lastly, we sum $P_{ind}(x,y)$ across the space to arrive at $\langle P_{ind} \rangle$, serving as a metric of

305   how much the FF enhancement at a given sounding is affected by heavy industry. Soundings with $\langle P_{ind} \rangle$ larger than the 75th or 90th percentiles are marked as locations "impacted" or "strongly impacted" by heavy industry within the city. Sensitivity and significance analyses are conducted and presented in **Sect. 3.2.2** to test if: 1) the results are subject to the percentile threshold for defining industry-dominant soundings, and; 2) ERs over industry-dominant soundings are statistically significantly different from the remaining soundings.

3   Results

310

        ER_{CO} values and uncertainties are reported at multiple spatial scales, originating from the spatially-explicit sounding-level (**Eq. 3**) to the overall overpass- and city- level. Again, only ERs at soundings within the urban plume are selected. Overpasses with too low valid soundings are also removed from the results. Before presenting ERs at different spatial scales, we assess the few factors that may influence the derived ER_{CO}.

315 ## 3.1   Interference factors that modify ER_{CO}

        We examine the impacts on ER_{CO} from the following interference factors: 1) differences in AKs between OCO-2/3 XCO_2 and TROPOMI XCO; 2) shifts in wind fields induced by asynchronous overpass times; and, 3) urban-background contrast in biogenic and pyrogenic contributions. In summary, we found that difference in AKs and wind directions between sensors can significantly affect the spatially-resolved ER_{CO}. After removing the overpasses substantially interfered by wind shift from

320   consideration, biogenic and pyrogenic contributions play a minor role in the overall overpass- or city-level ERs.

        The sensor-specific AKs and wind speed were incorporated into the calculation of species-specific column footprint in X-STILT as introduced in **Sect. 2.2**. By looking at the $\gamma_{foot} = \frac{\langle XF_{CO_2} \rangle}{\langle XF_{CO} \rangle}$ (**Supplementary Fig. S5d**), one can tell the impact on ER_{CO} due to mismatches in AKs and wind fields between sensors. For instance, γ_{foot} spans from 1.20 to 1.54 over Los Angeles and from 1.02 to 1.38 over Shanghai across different overpasses (printed in **Fig. 7**). γ_{foot} is generally larger than 1 because the

325   TROPOMI XCO AKs near the surface are less than 1 and smaller than OCO-2/3. Simply using enhancement ratios without accounting for mismatches in AK and wind speed between sensors will likely lead to an underestimation of the emission ratios (**Eq. 3**). On average, overpass-level ER_{CO} can be about 20% higher than the enhancement ratio for the examined cases.

        The second factor is the changes in wind directions between two overpass times (Δt), which is evaluated using the same approach for identifying the urban plumes in **Sect. 2.2.2**. Again, these colored contours and curves in **Fig. 5** do not indicate the

330   intensity of concentration nor flux fields (as no prior emission is used), but the likelihood of urban plumes solely determined by atmospheric dispersion. Matching between OCO-3 soundings and TROPOMI polygons as described earlier would be fine

for concurrent observations (e.g., "good cases" with almost identical plumes at two times in **Fig. 5a,b**); but problematic if Δt is large (e.g., "outliers" with significant changes in urban plumes in **Fig. 5e,f**). Since no simple wind or plume rotation would improve the ER estimates, cases with $\Delta t > 3$ hours are removed from this analysis. The cases between the "good cases" and the

335   "outliers" are cases to be used with caution (**Fig. 5c,d**). By comparing the overlap of plumes at the two times, we then shifted the OCO-3 soundings to better align with the TROPOMI polygons. For example, on Feb 20, 2020, because the modeled plume at the OCO-3 overpass time (06:06 UTC) appears northward compared to the plume at the TROPOMI overpass time (04:44 UTC), soundings at the OCO-3 overpass time were shifted southward by 0 to 2 grids (**Supplementary Fig. S6**). In other words, by shifting the observed FF XCO_2 enhancements, we better align the urban plume at OCO-3 time with the plume at TROPOMI

340   time. Every OCO-TROPOMI coincidence has been manually examined and assigned to one of the three categories, which are further summarized in **Sect. 4.1**.
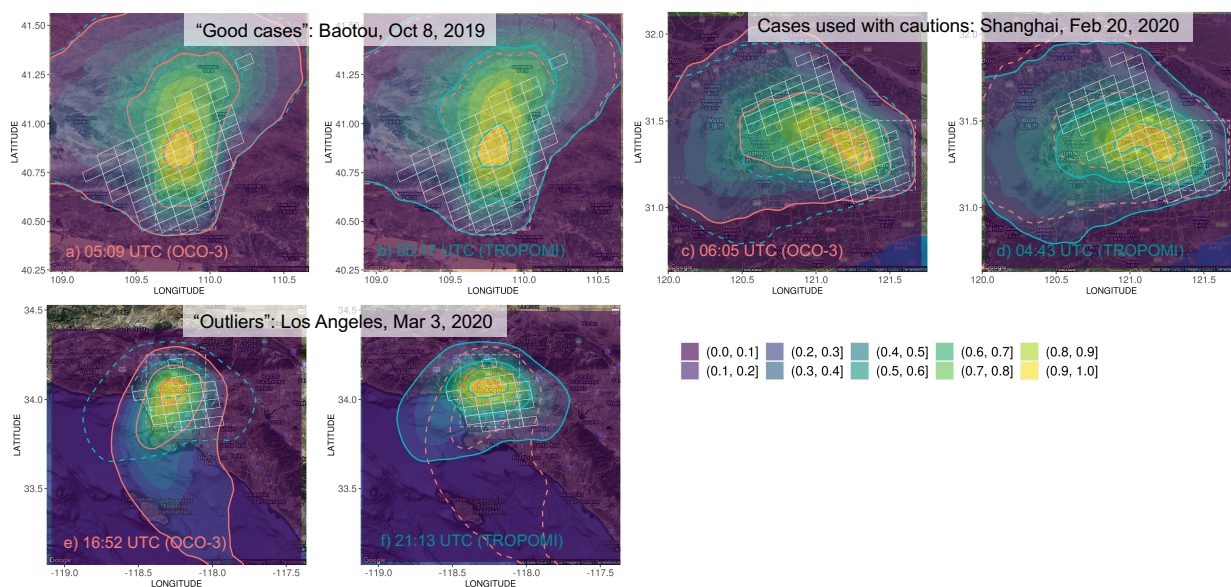

Figure 5. Examples of modeled urban plumes during OCO-3 (red curve) and TROPOMI (blue curve) overpass times (in UTC labelled on the bottom of each panel). The likelihood of these meteorology-only urban plumes (no emission involved) is quantified by the normalized KDE (10 intervals in the color legend) of modeled air parcel distribution (yellow-green-purple contours). Three types of overpasses are shown as follows: 1) "good cases" with almost identical urban plumes at two times, e.g., Baotou on Oct 8, 2019 with Δt of 8 mins (a, b); 2) cases to be used with caution where the urban plume shifts from one time to another and requires a simple plume rotation, e.g., Shanghai on Feb 20, 2020 with Δt of 1.5 hours (c, d); 3) outliers where the urban plumes change significantly, e.g., for Los Angeles on March 3rd, 2020 with Δt of over 4 hours (e, f). Outliers with Δt of over 3 hours are removed from the final results.

The last factor is the urban-background contrast due to non-FF sources/sinks. Although LA is surrounded by occasional intense wildfire activities, column anomalies due to biomass burning suggested by the coupling of GFAS and X-STILT are minimal for the dates we examined. However, since fire-related ER_{CO} are mostly higher than FF-related ER_{CO} (**Fig. 1**),

Atmospheric
Chemistry
and Physics
Discussions
Open Access
EGU

345 properly accounting for pyrogenic contributions and gradients in the enhancement is important for cities in mountainous and forested areas during the fire season (e.g., Mexico City and LA). The sounding-specific modeled biogenic XCO_2 anomalies using SMUrF and X-STILT ranges from -0.7 to 0.3 ppm depending on the season and the wind direction (**Supplementary Fig. S7**) and are further aggregated to the TROPOMI scale. As explained above, strong urban-background gradients in these biogenic anomalies (i.e., δX_{bio}) may alter the FF enhancement and ER_{CO}, so such gradients were used to correct the constant

350 background X_{bg}. Take the two overpasses with the largest urban-background contrast as examples: as biospheric uptake is normally weaker in urban areas than surrounding rural areas (often as background regions), the urban-rural gradient for locations in the plume region becomes more positive (**Supplementary Fig. S8b**). Nonetheless, even for the one summertime SAM over Zibo on June 21, 2020, sounding-level δX_{bio} ranges from 0 to 0.4 ppm, which remains small compared to sounding-level $FFCO_2$ enhancements of 2 to 7 ppm (**Supplementary Fig. S9a,b**). For most other overpasses, urban-background δX_{bio} re-

355 mains < 0.2 ppm. Even with a bias in the resultant δX_{bio} (resulting from uncertainties in prior NEE), the effect on derived FF enhancements and ER_{CO} would be small.

3.2 Intra-city ER_{CO} variations and signal from heavy industry

The measured concentration enhancements are the net consequence of associated sources/sinks from source regions. That is, high atmospheric content of CO_2 or CO at the sounding location does not necessarily indicate a high emission rate at this

360 location (Kiel et al., 2021). Our derived emissions and ERs, although reported for each sounding, indicate the overall emission and combustion efficiency over its source region.

In the following subsections, we present ERs from sounding-level to the overpass- and city-level. Since aggregating spatially-explicit sounding-level ERs to a single value per overpass or city is sensitive to the adopted method/statistics and the overpass-specific atmospheric movement, we bootstrapped ECO and ECO_2 based on sounding-level emissions and uncertainties 5,000

365 times and applied linear regression fits (e.g., light grey lines in **Fig. 6**). Specifically, 5,000 random sets of ECO and ECO_2 were generated following assumed normal distributions, where sounding-level emissions denote the mean statistic with observed and background uncertainties as the standard deviation (SD) statistic. We used the standardized major axis (SMA) solution for linear regression to minimize the deviation of the data point from the regression line for both axes. Eventually, we obtained 5,000 bootstrapped slopes and only selected slopes with positive values, of which mean values and SDs yield the overpass-level

370 ER_{CO} values and uncertainties (colored dashed lines and text in **Fig. 6**). Sounding-level ER_{CO} values from all overpasses are also presented in histograms, which generally follow a log-normal distribution (**Figs. 7b**, **7d**).

3.2.1 Baotou and Zibo

Combustion efficiencies are generally poor for these two industry-oriented cities. The overpass-specific ERs span from 8.1±1.3 to 26.7±3.8 mmol mol^{-1} with an integrated city-level estimate of 18.4±0.6 mmol mol^{-1} for Baotou (**Fig. 6a**). According to

375 GID, the Baotou iron and steel group is located in the city and contributes to an annual capacity of crude iron of 12,618.91 kt with estimated CO_2 emissions of 20,462 kt per year. The relative low ER_{CO} and FF enhancements in Feb 2021 coincides with the timing of the Spring Festival in 2021. SDs of the bootstrapped slopes are higher for overpasses with fewer high-quality

satellite soundings, e.g., 3.8 mmol mol^{-1} for overpasses with 7 available urban TROPOMI polygons over Baotou on May 31, 2020, which helps minimize the impact of low sounding numbers on overall city-level ER estimates.
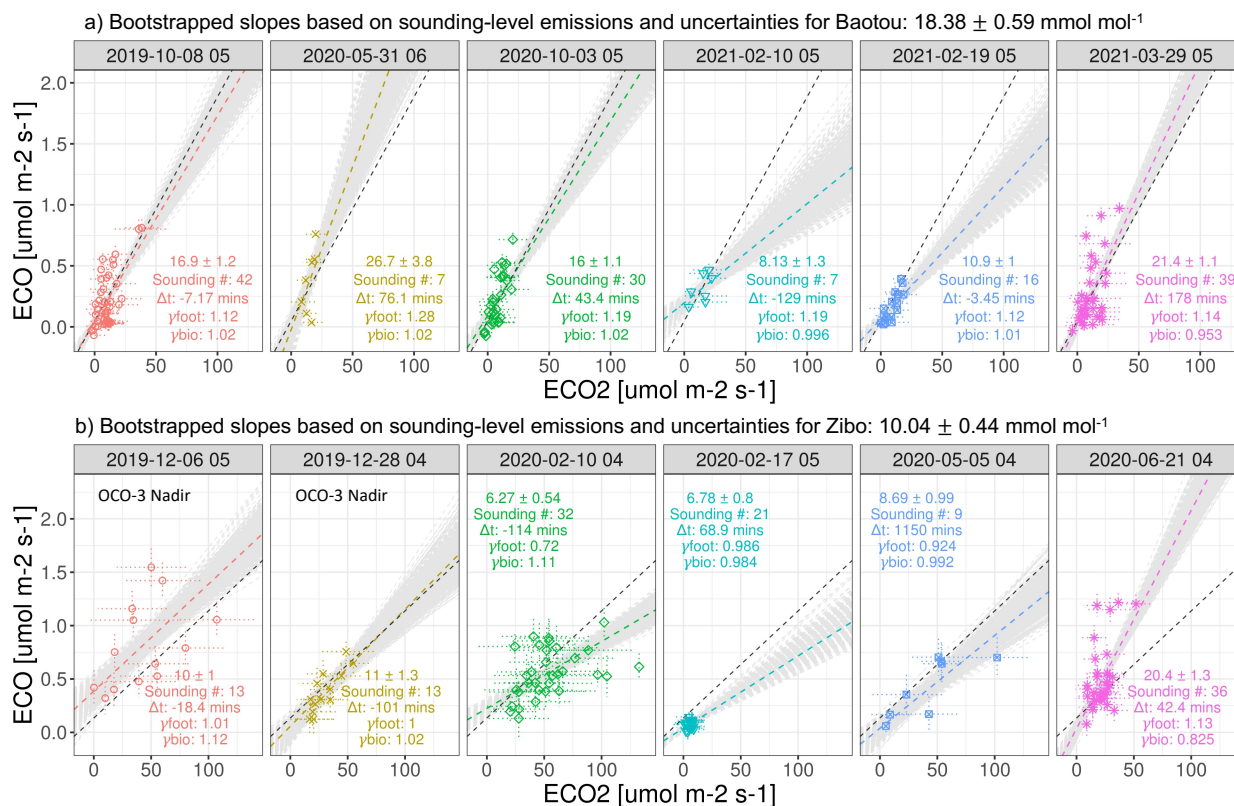

Figure 6. Scatter plot of CO and CO_2 fluxes [μmol m^{-2} s^{-1}] and their uncertainties (error bars) for Baotou (a) and Zibo (b). Data for all overpasses are from OCO-3 SAMs, except for the first two overpasses for Zibo (OCO-3 Nadir). Linear regressions using the standardized major axis (SMA) method are applied for the data from each overpass (dashed colored lines) and all overpasses (dashed black line). Only bootstrapped regression lines with positive slopes were chosen from the Monte Carlo experiment (dashed gray lines). TROPOMI overpass time in UTC, total TROPOMI sounding numbers, discrepancies in overpass time between OCO and TROPOMI (Δt), impacts from AK and atmospheric transport between sensors (γ_{foot}) and urban-rural biogenic gradient (γbio) are labelled on each panel. XCO_2 on Dec 6 and Dec 28, 2019 over Zibo are the Nadir OCO-3 observations. Feb to May in 2020 is the time frame for the initial phase of the COVID-19 lockdown in China.

380   Interestingly, the ER for Zibo first dropped from 11.0 ± 1.3 mmol mol^{-1} to 6.3 ± 0.5 mmol mol^{-1} during Feb 2020 and then gradually rose back to 20.4 ± 1.3 mmol mol^{-1} by June 2020 (**Fig. 6b**). In addition to low ER$_{CO}$ in Feb and May 2020, their FF enhancements remain low. Such temporal variations in both ER$_{CO}$ and enhancements agree nicely with the timing of the initial phase of COVID-19 lockdown in China (e.g., Laughner et al., 2021).

3.2.2 Los Angeles and Shanghai

385 Although OCO-3 has sampled the Los Angeles basin several times to date, unfortunately, a few of them did not pass the quality check and were removed from the final result due to their dramatic change in wind direction (e.g., > 3 hours time difference on March 3, April 15, and May 5, 2020 for LA, see discussion in **Sect. 4.1**). The overpass-level ER ranges from 7.2±0.8 to 12.4±1.3 mmol-CO/mol-CO$_2$ with a city-level value of either 9.7±0.5 mmol mol^{-1}informed by the regression approach (**Fig. 7a**) or 9.9 mmol mol^{-1}by the histogram approach (**Fig. 7b**). Our space-based ER$_{CO}$ values for LA fall within the range of 7.1

390 to 12.4 mmol mol^{-1}inferred from several prior studies (Wennberg et al., 2012; Brioude et al., 2013; Hedelius et al., 2016; Silva and Arellano, 2017), despite the time difference. Small discrepancies in ER$_{CO}$ between studies may be attributed to discrepancies in time of interest, sampling strategies, and techniques for calculating ER$_{CO}$ (e.g., exact background locations). In contrast to LA, where urban plumes are usually well-constrained with the basin, the wind speeds and directions change dramatically among different overpasses over Shanghai —i.e., southeasterly wind on Feb 4 and Feb 20, 2020, southwesterly wind on Feb

395 24, 2020 and Feb 19, 2021 and northerly wind on April 23 and Dec 30, 2020. Such changes in the wind regimes between overpasses over Shanghai suggest that observations per overpass reflect fluxes over different source regions, which emphasizes the importance of integrating atmospheric transport in interpreting temporal variations in observation-based ERs. The overpass-specific ER ranges from 4.7±1.2 to 20.1±7.3 mmol mol^{-1}with a city-level average of 10.5±0.4 mmol mol^{-1}based on the linear regression approach (**Fig. 7c**).

400 Histograms for the sounding-level ERs within the LA basin and the greater Shanghai area are shown in **Fig. 7b,d**, respectively. As described earlier, to address the overpass-specific meteorology, we coupled the LZC-based industrial coverage with X-STILT column footprints to locate the soundings affected or strongly affected by heavy industry in a city. For example, on Feb 20, 2020 the few soundings with $\langle P_{ind} \rangle$ of > 75th percentiles (outlined in black in **Supplementary Fig. S5**) are identified as soundings affected by industry.

405 Heavy industrial regions within the LA basin are concentrated to the south (e.g., the Port of LA) and to the west of downtown (**Fig. 4e**). The distribution of ERs for industry-dominant soundings tend to shift slightly towards the lower end (blue or red bars in **Fig. 7b**) compared to the distribution for all soundings (black bars in **Fig. 7b**). Specifically, ERs > 20 ppb ppm^{-1}are less frequently found for industry-dominant soundings (red bars in **Fig. 7b**). It is worth noting that the industry-oriented soundings have slightly lower CO but higher CO$_2$ enhancements (**Supplementary Fig. S5a,b**), compared to all soundings within the

410 valley, resulting in slightly lower ER$_{CO}$ (**Supplementary Fig. S5c**). No iron and steel facilities or coal-fired power plants are found over the heavy industry area in LA according to GID and GEM. We hypothesize that the slight shift of ER$_{CO}$ towards the lower end may be explained by the heavy-duty diesel engines and natural gas power plants occupying the Port of LA versus the predominately gasoline vehicles across the city, because ER$_{CO}$ for heavy-duty diesel vehicles and non-coal-fired power plants are generally lower than that for light-duty gasoline vehicles. For example, by splitting observations for daytime versus

415 nighttime, a field campaign in 2007 in Beijing suggested that the ER linked to nighttime diesel transportation is much lower than the gasoline sub-sector (Westerdahl et al., 2009, **Fig. 1a**). Similar to LA, higher fuel efficiency has been found over the ship channel of Houston (ER of ∼4 ppb ppm^{-1}) compared to downtown Houston (ER of ∼10 ppb ppm^{-1}) (Brioude et al.,
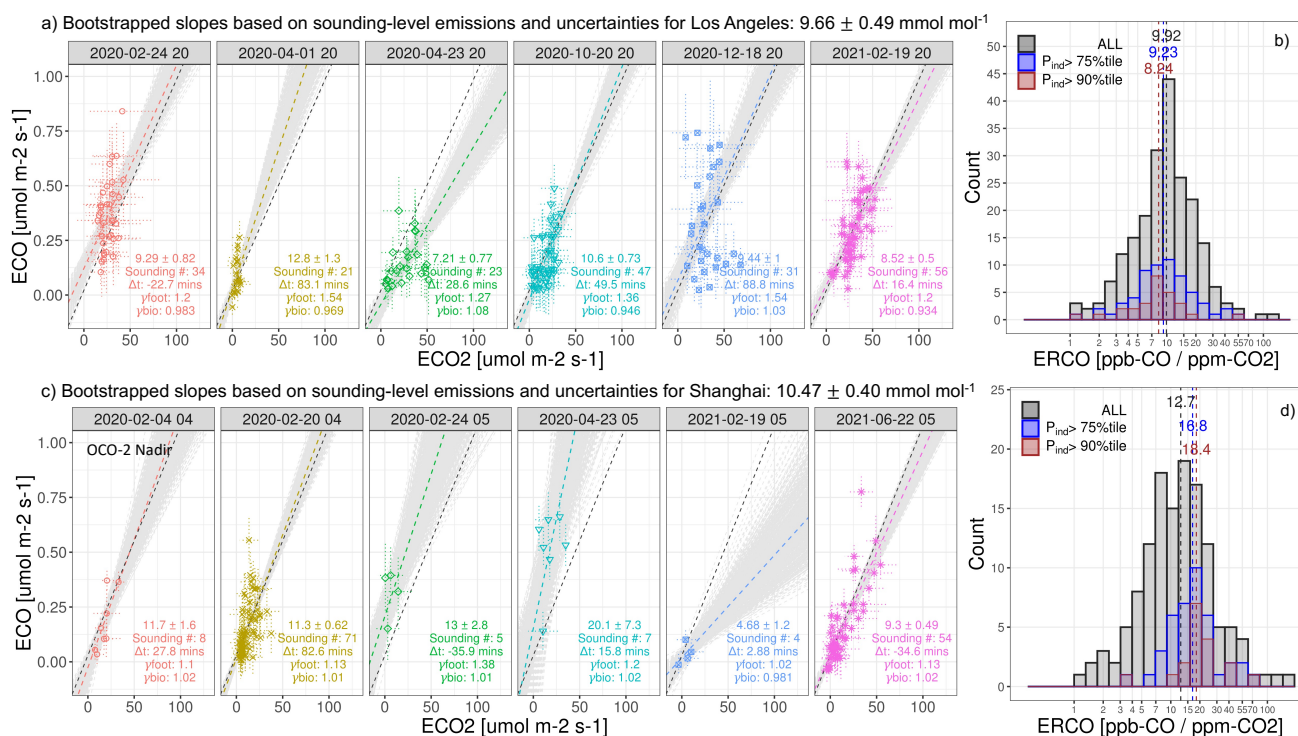
Figure 7. a, c) Same as **Fig. 6** but for LA and Shanghai. Only bootstrapped regression lines with positive slopes are presented as light grey lines. b, d) Histogram of ER_{CO} for all soundings (black bars); soundings impacted or strongly impacted by heavy industry are defined using $\langle P_{ind} \rangle$ larger than their 75th or 90th percentiles (blue or red bars) with corresponding median ERs (vertical dashed lines). The industrial impact is quantified using column footprints from X-STILT (to inform atmospheric transport) together with localized information from the urban land cover data WUDAPT.

2012, **Fig. 1b**). Unfortunately, only two good SAMs are available near Houston from late 2019 to June 2021, but future work can further validate the urban-industry contrast in ERs from space.

420   For Shanghai, the heavy industry is concentrated to the north of the city center (**Fig. 4a**). Interestingly, in contrast to LA, ERs strongly concentrated with heavy industry are skewed towards the higher end with medians of 16.8 or 18.4 ppb ppm^{-1}(blue or red bars in **Fig. 7d**), compared against the city-level median of 12.7 ppb ppm^{-1}(black bars in **Fig. 7d**). FFCO and FFCO$_2$ enhancements and ER_{CO} are all higher for industry-oriented soundings than those for all soundings combined. Such spatial divergence in enhancements and ERs may be attributed to substantial CO emissions from iron and steel production. During

425   such production processes, iron ores are reduced to crude iron and steel where CO is involved. According to the plant level estimate in 2019 from GID, Baoshan Iron & Steel Co., Ltd. located to the north of downtown Shanghai has an annual crude steel capacity of 25,099.4 kt yr^{-1} and a total CO$_2$ emission of 32,148.0 kt yr^{-1} for all coke, sinter, iron, and crude steel combined.

Finally, to validate the ER shifts related to heavy industry within an urban area, we tested different percentile thresholds other than the default 75th and 95th for determining industry-dominant soundings (**Sect. 2.3**). The above statements on industry-

430   impacted ER_{CO} hold if using alternative thresholds including the 50th, 60th, 80th percentiles. Additional Welch two-sample t-test confirms that ERs from industry-dominant soundings significantly differ from the remaining soundings (i.e., less affected by industry). When the adopted percentile threshold increases from 50th to 95th, divergence in ERs between industrial vs. non-industrial soundings becomes more apparent and the p-value for statistical significance in such difference becomes smaller (p-values < 0.05). Also, the average number of OCO-3 soundings in a TROPOMI polygon is roughly the same for industry-

435   affected soundings versus the rest (e.g., 11.8 vs. 10.3 for LA and 7.3 vs. 8.7 for Shanghai).

     We note that it is difficult to separate individual sectoral signals purely from observations (without prior assumptions on sectoral contributions), since atmospheric concentration at a given location is comprised of various underlying burning processes spread over the source region. Even using additional co-emitted species, it would be risky to assume that a co-emitted species (e.g., NO_x) solely comes from one individual emission sector.

440   ## 4   Discussion

This study is one of the first to analyze intra-city variations of emission ratios between CO and CO_2 using two asynchronous satellite sensors. We describe 1) complications induced by discrepancies between satellite sensors and retrievals and 2) demonstrate methods to mitigate these complications by accounting for species-specific averaging kernels and urban-background contrast in non-FF sources/sinks using an atmospheric transport model.

445   ### 4.1   Influence from non-FF components and atmospheric transport

The pyrogenic anomalies are minimal for the overpasses we examined, but should be considered for certain cities considering the high ER_{CO} from forest wildfires of 35 to 80 ppb ppm^{-1}(**Fig. 1a**). Most overpasses we analyzed fall within the dormant seasons. For the three overpasses during the growing season, modeled biogenic anomalies using the SMUrF model for a given OCO-2/3 sounding may reach up to 0.5 ppm (**Supplementary Fig. S7**). Even though modeled NEE and resultant biogenic

450   contributions/gradient can be uncertain, we stress again it is the urban-background biogenic contrast (δX_{bio} in **Eq. 1**) that should be considered for when estimating FFCO$_2$ enhancements given our setup for background value. Satellite missions such as TROPOMI and the upcoming Geostationary Carbon Cycle Observatory (GeoCarb) will also provide the Solar-Induced Fluorescence (SIF), which may help improve spatially-explicit SIF-based GPP and NEE estimates (Turner et al., 2020; Wu et al., 2021), specifically by reducing the dependence on other remote sensing products and the assumption of model parameters

455   for each plant function type.

     The biggest challenge interfering the robust spatially-resolved ER estimates is the wind directional shift induced by the lack of concurrence between sensors. Substantial changes in the wind direction and resultant urban plumes (e.g., the "outlier" case in **Fig. 5e,f**) were mostly found for overpasses when absolute time differences $|\Delta t|$ were > 2 hours (implied by the bars with white strips and asterisk on top in **Fig. 8**). However, if TROPOMI pixel sizes are relatively large (i.e., non-nadir observations)

460   or the wind is steadier, this $|\Delta t|$ constraint can be relaxed. For instance, TROPOMI polygon sizes for Baotou on May 31, 2020 are sufficiently large compared to the shift in urban plumes despite its $|\Delta t|$ of 3 hours (**Fig. 8**). Because of this, we decided to

exclude overpasses with |Δt | > 3 hours. In addition, we manually re-positioned the OCO-3 soundings to TROPOMI polygons
for a few cases (bars with non-zero numbers on top in **Fig. 8**) using a simple wind/plume shift demonstrated in **Sect. 3.1**).
Fortunately, future geostationary satellite will be capable of mapping XCO and XCO_2 spontaneously at a higher temporal

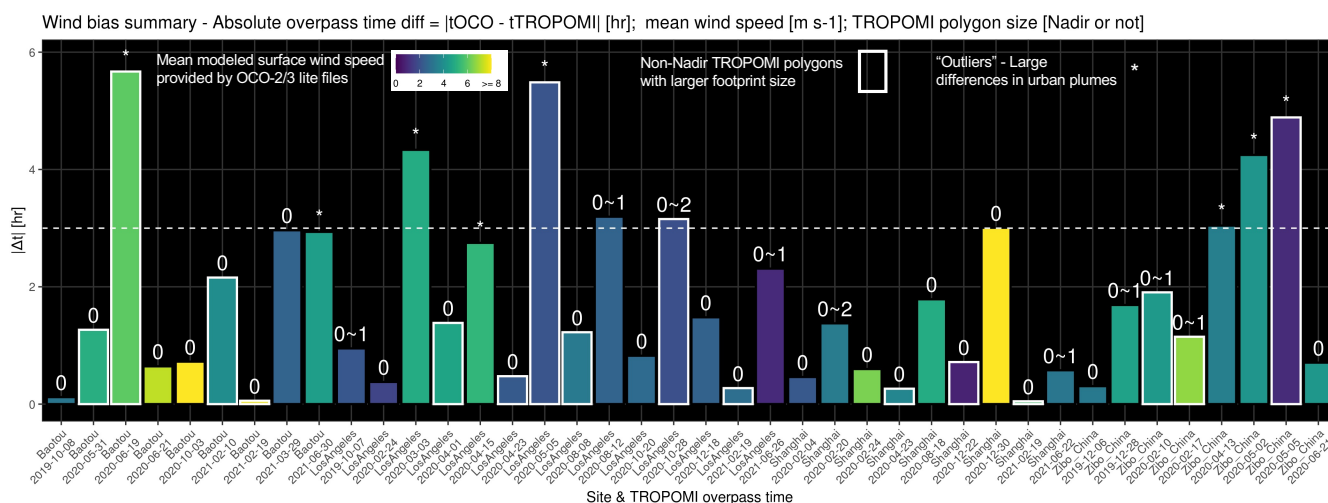465 frequency, which will eliminate this issue.

Figure 8. A summary figure of the investigation on the wind directional shift between OCO-2/3 versus TROPOMI overpass times. The y-axis denotes
the absolute time difference (Δt in hours) for multiple overpasses. The colors of the bars represent the instantaneous modeled surface wind speed [m s^{-1}]
provided by OCO-2/3 Lite files. Bars labelled with an asterisk indicate the urban plumes between two times differ significantly that a simple plume rotation
fails to fix. The number on each bar denotes the number of TROPOMI polygons needed to be shifted to align the urban plumes at two times. "Good Cases" do
not require a manual plume shift (bars with zero labelling). Bars outlined in white indicate that the sampled TROPOMI soundings on that date are non-nadir
with larger pixel size.

4.2 ERs per sounding, per overpass, and per city

Contrary to previous work relying on inventory-based sector-based ERs, we attribute the intra-urban gradient to heavy industry
using a urban land cover classification dataset. Such high-resolution localized maps help guide the identification of observations
strongly influenced by heavy industry. Based on a limited sample size, the heavy industry within the greater Shanghai area is

470 tied to an ER_{CO} higher than the city average reflecting a poor combustion efficiency (**Fig. 7d**). Industry-oriented cities like
Baotou and Zibo are less efficient in their burning activities. In particular, industry-dominant ERs over Shanghai (20.9 mmol
mol^{-1} as indicated by the red bars in **Fig. 7d**) align better with the overall city-scale ER over Baotou or Zibo (24.1 or 20 mmol
mol^{-1}, **Fig. 6**). The previously reported urban-integrated ER_{CO} values are mostly constrained within the range of 5 to 20 ppb
ppm^{-1} with a few exceptions over 30 ppb ppm^{-1} in east Asia before 2010 (**Fig. 1**). The order of magnitude of our city-level

475 estimates from space agree well with that of previously reported ERs.

Atmospheric
Chemistry
and Physics
Discussions

Reporting one city-scale ER_{CO} from spatially-explicit ERs can be subjective to 1) the adopted statistics, 2) the overpasses and their associated wind regimes, and 3) estimated uncertainties in ER_{CO}. For example, overall ER based on all soundings within the urban plume differs from ERs from a selection of soundings. ERs between overpasses over Shanghai can vary due to changes in the wind fields and source-receptor geometry. Even though we begun with all available OCO-2/3 observations in a SAM, only soundings located within the urban plumes (black curve in **Fig. 3**) are selected for ER estimates, which is an unbiased way to assess different overpasses with different meteorological conditions. The mean or median value of sounding-level ER_{CO} (e.g., 13.4 or 9.6 ppb ppm^{-1} for LA in **Supplementary Fig. S10**) differs from the city-average when using the regression slope method that take observational uncertainties into account (e.g., 10.59 ppb ppm^{-1} for LA in **Fig. 7a**). Apart from these bulk quantities, intra-city distributions of ERs are negatively-skewed in the linear space and roughly follow the normal distribution in natural log-space (**Supplementary Fig. S10**), where a few observations with higher ER_{CO} are influenced by point sources with poorer combustion efficiency. More observations with finer satellite pixels across the city would improve the robustness in both the spatial distribution and the bulk estimates of ERs.

4.3 Limitation and implications

The main limitation of this work is the relatively low sample size. When more satellite data become accessible, intra-city ERs can be used to more robustly re-assess the temporal variations in sector-oriented combustion efficiency, including across different seasons and business-as-usual scenarios versus pandemic-disturbed time frames. Beyond the sheer number of soundings, uncertainty arises due to the aggregation of CO_2 enhancements from the finer resolution OCO-3 grid to coarser TROPOMI spatial scale. The centered lat/lon coordinates of OCO-2/3 soundings are used to decide which corresponding TROPOMI polygon they fall into, while a very few OCO soundings may locate right on the boundary of TROPOMI polygons. Nevertheless, we find no significant bias associated with the number of OCO soundings per TROPOMI polygon. The XCO_2 variability from different OCO soundings within a given TROPOMI polygon serves as the "observational noise" in the uncertainty analysis.

We then discuss the impact on our results given the lack of consideration of the secondary CO source from both anthropogenic and biogenic VOCs (AVOCs, BVOCs). Under a cascade of reactions in favorable conditions, VOCs can be oxidized to CO at various rates, relying on the amount, speciation, and reactivity of VOCs. The lifetimes of CH_4 and certain VOCs species against OH radical are long enough compared to our time of interests, i.e., a few hours before overpass time to render their impact negligible in this analysis. BVOCs (e.g., isoprene) and a subset of the anthropogenic VOCs (e.g. alkenes) react quickly and often generate HCHO (e.g., Surl et al., 2018) which subsequently can be photochemically converted to CO in a few hours. For example, isoprene contributed to 21.2% of the total CO sources from June to August, but negligible amount from March to April over Alaska (Miller et al., 2008). Most of our overpasses fall within the non-growing season, the CO produced by BVOCs may likely be encapsulated in the background XCO and yield a small impact on our results. Regarding industrial areas with possible higher AVOCs than urban cores, e.g., over Houston in Aug 2000 (Czader et al., 2008), whether AVOCs produce significantly more CO over industrial areas than urban cores within the time period of interest remains unclear. Owing to the lack of observations for the VOC composition and species-specific emissions in the air mixture over different cities and parts

of a city, it is challenging to accurately quantify the intra-city variation in secondary CO production and isolate such variation
510   from the observed XCO variability.

This work also provides some insights towards estimating emission ratios from future satellite sensors, as ERs help pinpoint
hotspots with poor combustion efficiency can help inform sub-city emission/pollution control efforts.

Satellite-based ER may help evaluate sectoral emission factors and source locations adopted in bottom-up emission inven-
tory. Substantial contrast in both the magnitude and spatial distribution of enhancement ratios can be found between the obser-
515   vations and forward simulations based on X-STILT column footprint and sectoral emissions from EDGARv5. Over Shanghai,
for example, enhancement ratios simulated using the industry emissions from EDGAR are located far south (**Supplementary
Fig. S11c**), compared to the observed enhancement ratio in **Supplementary Fig. S11a**. Additionally, the simulated enhance-
ment ratios (**Supplementary Fig. S11b**) are generally too high (e.g., > 50 ppb ppm^{-1}) compared to observed ratios (mostly $<$
30 ppb ppm^{-1}). Such model-data mismatch may result from inaccurate activity data and emission factors when constructing
520   the bottom-up flux estimates as well as from uncertainties in the atmospheric transport. The simple example illustrates that
satellite observations of trace gases could be used to evaluate emission factors used in bottom up emission inventory. More
sophisticated approaches such as flux inversion (Hedelius et al., 2018; Brioude et al., 2011, 2012; Palmer et al., 2006) may
facilitate the constraint of sector-specific CO and CO_2 emissions.

Spatial proxies including nightlight data from the Black Marble (https://blackmarble.gsfc.nasa.gov/) and detailed urban
525   land cover data can not only support the development of emission inventories but also sector-orientated investigations with
mapped atmospheric concentrations of CO_2 and co-emitted pollutants from space. This work demonstrates the benefit of using
high-resolution urban land cover datasets like WUDAPT in informing locations of various anthropogenic activities, building
structures, and vegetation coverage. Yet, such high-resolution urban datasets (like WUDAPT and NLCD) are currently only
available for a limited number of cities across the globe.

530   ## 5   Conclusion

We investigated fossil fuel combustion efficiency by quantifying the emission ratio of CO and CO_2 across Los Angeles, Shang-
hai, Baotou, and Zibo, using nearly coincident observations of TROPOMI XCO and OCO-2/3 XCO_2. The multiple swaths of
observations collected by OCO-3 SAMs cover a much broader area relative to OCO-2 swaths, facilitating the determination of
background values. We incorporate spatial gradients in the background values by calculating the background for each swath
535   and correcting for the urban-background gradient due to non-anthropogenic sources and sinks. Sensor-specific averaging ker-
nel profiles and meteorological conditions were accounted for using an atmospheric transport model (X-STILT). The ratio
between XCO and XCO_2 enhancements without considering such sensor-specific factors is normally lower than the emission
ratio. Cases with severe asynchronicity, specifically overpass time differences over 3 hours, are excluded from the final result.
Temporal variations in the wind fields may result in different source regions with respect to the satellite soundings. Therefore,
540   properly accounting for the meteorology or the source-receptor relation and identifying the soundings affected by the urban

Atmospheric
Chemistry
and Physics
Discussions
Open Access
EGU

emissions is important, which is the main reason that an atmospheric transport model is used to identify soundings strongly affected by heavy industry.

The overall city-level ER_{CO} for Shanghai (10.5 ± 0.4 mmol mol^{-1}) is slightly larger than the city-level ER_{CO} for Los Angeles (9.7 ± 0.5 mmol mol^{-1}). Looking at the sub-city scale, industry-related ER_{CO} are much larger than the city-level
545 ER_{CO} for Shanghai; whereas industry-related ER_{CO} slightly lower than the city-level ER_{CO} for LA. This divergence in ERs is likely driven by the distinct industrial processes between the two megacities. ERs tied to heavy industry regions in Shanghai (18.4 mmol mol^{-1}) are approximately equal to the city-level ER_{CO} for the industry-orientated city of Baotou (18.4 ± 0.6 mmol mol^{-1}). High ERs highlight the poor burning efficiency tied to industrial activities, e.g., high CO emissions from metal production.

550 With future satellites providing better spatial and temporal coverage of XCO_2, XCO, and other relevant co-located observations, it may be possible to monitor and verify temporal trend or variations in combustion efficiencies for hotspots within an urban area, which has significant implications for urban planning and emission control.

Code and data availability. OCO-3 L2 B10r XCO_2 data and TROPOMI XCO data were accessed from https://doi.org/10.22002/D1.2046 and 10.5270/S5P-1hkp7rp, respectively. X-STILT code has been modified to work with TROPOMI data archived on github branch at
555 https://github.com/uataq/X-STILT. We kindly ask the users to follow the code policy in utilizing and acknowledging the X-STILT code for interpreting TROPOMI column data. Hourly NEE fluxes from SMUrF are archived on Oak Ridge National Lab DAAC at https://doi.org/10.3334/ORNLDAAC/1899.

Appendix A: List of prior studies collected in Figure 1

Sector in **Fig. 1a**	Location	Years	Reference	Additional notes
Traffic	Denver, US	1997	Bradley et al. (2000)	
Traffic	Switzerland	2004	Vollmer et al. (2007), Table 2	Gubrist Tunnel
Traffic	CONUS	2005-2007	Bishop and Stedman (2008)	Chicago, Denver, Los Angeles, Phoenix
Traffic	Paris	2012	Ammoura et al. (2014), Table 2	Tunnel (congestion vs. moving)
Traffic	Switzerland	2011	Popa et al. (2014), Table 1	Islisberg Tunnel (moving)
Traffic	Beijing, China	2007	Westerdahl et al. (2009)	diesel heavy-duty vs. gasoline light-duty
Shipping	China	2011	Zhang et al. (2016), Table 3	Diesel engines; Estimated from EFs
Shipping	Western Europe	2007	Moldanová et al. (2009), Table 5	Diesel engine; Estimated from EFs
Shipping	Texas	2006	Williams et al. (2009), Figure 2	Diesel engines; Estimated from EFs
Biofuel + FF	SE Asia	2007	Lai et al. (2010), Table 2	
Biofuel + FF	Asia	2000	Russo et al. (2003), Table 9	Central, Coastal, SE and WSW Asia
Biomass burning	Global	NA	Akagi et al. (2011), Table 1-2	Estimated from EFs

Urban areas in **Fig. 1b**	Observation years	Reference
Los Angeles (LA)	2002 and 2010	Brioude et al. (2013)
LA	2007-2008	Djuricin et al. (2010)
LA	2008 and 2010	Wennberg et al. (2012)
LA	2010	Silva et al. (2013); Silva and Arellano (2017)
LA	2013-2016	Hedelius et al. (2016)
LA	2019-2021	**This study**, Figure 7
Pasadena	2007	Wennberg et al. (2012), Table 2
Sacramento	2009	Turnbull et al. (2011a), Sect. 3.2
Indianapolis (Indy)	2012-2014	Turnbull et al. (2015)
Salt Lake City (SLC)	2015-2016	Bares et al. (2018), Table 2
Edinburgh	2005	Famulari et al. (2010), Table 1
Paris	2010	Lopez et al. (2013)
Paris	2010-2014	Ammoura et al. (2016), Table 1
London	2006	Harrison et al. (2012), Figure 27
London	2012	O'Shea et al. (2014), Table 3
London	2016	Pitt et al. (2019), Table 2
Rotterdam	2011	Super et al. (2017)
Germany Alps	2012-2013	Ghasemifard et al. (2019)
Hungary	2017	Haszpra et al. (2019), Table 1
St. Petersburg	2019	Makarova et al. (2021)
Miyun	2004-2008	Wang et al. (2010), Table 2
Beijing	2006	Han et al. (2009), Figure 11
Shangdianzi	2009-2010	Turnbull et al. (2011b)
Nanjing	2011	Huang et al. (2015), Sect. 3.4.2
Seoul	2016	Tang et al. (2018), Table 3
Seoul	2019	Sim et al. (2020), Table 2
Jingdezhen	2017-2018	Xia et al. (2020), Table 3
Zibo, Baotou, Shanghai	2019-2021	**This study**, Figures 6-7

Atmospheric
Chemistry
and Physics
Discussions

565 *Competing interests.* The authors declare no conflict of interests.

Atmospheric
Chemistry
and Physics
Discussions

References

Akagi, S., Yokelson, R. J., Wiedinmyer, C., Alvarado, M., Reid, J., Karl, T., Crounse, J., and Wennberg, P.: Emission factors for open and
domestic biomass burning for use in atmospheric models, Atmospheric Chemistry and Physics, 11, 4039–4072, 2011.

Ammoura, L., Xueref-Remy, I., Gros, V., Baudic, A., Bonsang, B., Petit, J. E., Perrussel, O., Bonnaire, N., Sciare, J., and Chevallier, F.:
Atmospheric measurements of ratios between CO_2 and co-emitted species from traffic: A tunnel study in the Paris megacity, Atmospheric
Chemistry and Physics, 14, 12 871–12 882, https://doi.org/10.5194/acp-14-12871-2014, 2014.

Ammoura, L., Xueref-Remy, I., Vogel, F., Gros, V., Baudic, A., Bonsang, B., Delmotte, M., Té, Y., and Chevallier, F.: Exploiting stagnant
conditions to derive robust emission ratio estimates for CO_2 , CO and volatile organic compounds in Paris, Atmospheric Chemistry and
Physics, 16, 15 653–15 664, https://doi.org/10.5194/acp-16-15653-2016, 2016.

Bares, R., Lin, J. C., Hoch, S. W., Baasandorj, M., Mendoza, D. L., Fasoli, B., Mitchell, L., and Stephens, B. B.: The wintertime covariation
of CO_2 and criteria pollutants in an urban valley of the Western United States, Journal of Geophysical Research: Atmospheres, 123,
2684–2703, 2018.

Bishop, G. A. and Stedman, D. H.: A decade of on-road emissions measurements, Environmental Science & Technology, 42, 1651–1656,
2008.

Bradley, K. S., Brooks, K. B., Hubbard, L. K., Popp, P. J., and Stedman, D. H.: Motor vehicle fleet emissions by OP-FTIR, Environmental
Science and Technology, 34, 897–899, https://doi.org/10.1021/es9909226, 2000.

Brioude, J., Kim, S. W., Angevine, W. M., Frost, G. J., Lee, S. H., McKeen, S. A., Trainer, M., Fehsenfeld, F. C., Holloway, J. S.,
Ryerson, T. B., Williams, E. J., Petron, G., and Fast, J. D.: Top-down estimate of anthropogenic emission inventories and their in-
terannual variability in Houston using a mesoscale inverse modeling technique, Journal of Geophysical Research Atmospheres, 116,
https://doi.org/10.1029/2011JD016215, 2011.

Brioude, J., Petron, G., Frost, G. J., Ahmadov, R., Angevine, W. M., Hsie, E. Y., Kim, S. W., Lee, S. H., McKeen, S. A., Trainer, M.,
Fehsenfeld, F. C., Holloway, J. S., Peischl, J., Ryerson, T. B., and Gurney, K. R.: A new inversion method to calculate emission inventories
without a prior at mesoscale: Application to the anthropogenic CO_2 emission from Houston, Texas, Journal of Geophysical Research
Atmospheres, 117, https://doi.org/10.1029/2011JD016918, 2012.

Brioude, J., Angevine, W. M., Ahmadov, R., Kim, S. W., Evan, S., McKeen, S. A., Hsie, E. Y., Frost, G. J., Neuman, J. A., Pollack, I. B.,
Peischl, J., Ryerson, T. B., Holloway, J., Brown, S. S., Nowak, J. B., Roberts, J. M., Wofsy, S. C., Santoni, G. W., Oda, T., and Trainer,
M.: Top-down estimate of surface flux in the Los Angeles Basin using a mesoscale inverse modeling technique: Assessing anthropogenic
emissions of CO, NOx and CO_2 and their impacts, Atmospheric Chemistry and Physics, 13, 3661–3677, https://doi.org/10.5194/acp-13-
3661-2013, 2013.

Chandra, N., Lal, S., Venkataramani, S., Patra, P. K., and Sheel, V.: Temporal variations of atmospheric CO_2 and CO at Ahmedabad in
western India, Atmospheric Chemistry and Physics, 16, 6153–6173, https://doi.org/10.5194/acp-16-6153-2016, 2016.

Ching, J., Mills, G., Bechtel, B., See, L., Feddema, J., Wang, X., Ren, C., Brousse, O., Martilli, A., Neophytou, M., et al.: WUDAPT: An
urban weather, climate, and environmental modeling infrastructure for the anthropocene, Bulletin of the American Meteorological Society,
99, 1907–1924, 2018.

Crisp, D., Fisher, B., O'Dell, C., Frankenberg, C., Basilio, R., Bösch, H., Brown, L., Castano, R., Connor, B., Deutscher, N., et al.: The
ACOS CO 2 retrieval algorithm–Part II: Global X CO 2 data characterization, Atmospheric Measurement Techniques, 5, 687–707, 2012.

Atmospheric
Chemistry
and Physics
Discussions

Czader, B. H., Byun, D. W., Kim, S.-T., and Carter, W. P.: A study of VOC reactivity in the Houston-Galveston air mixture utilizing an
extended version of SAPRC-99 chemical mechanism, Atmospheric Environment, 42, 5733–5742, 2008.

Demetillo, M. A. G., Harkins, C., McDonald, B. C., Chodrow, P. S., Sun, K., and Pusede, S. E.: Space-Based Observational Constraints on
NO2 Air Pollution Inequality From Diesel Traffic in Major US Cities, Geophysical Research Letters, 48, e2021GL094 333, 2021.

Djuricin, S., Pataki, D. E., and Xu, X.: A comparison of tracer methods for quantifying CO_2 sources in an urban region, Journal of Geophys-
ical Research Atmospheres, 115, https://doi.org/10.1029/2009JD012236, 2010.

Duncan, B. N., Lamsal, L. N., Thompson, A. M., Yoshida, Y., Lu, Z., Streets, D. G., Hurwitz, M. M., and Pickering, K. E.: A space-
based, high-resolution view of notable changes in urban NOx pollution around the world (2005–2014), Journal of Geophysical Research:
Atmospheres, 121, 976–996, 2016.

Eldering, A.: OCO-3 B10 QTS Evaluation XCO2 Lite Files, https://doi.org/10.22002/D1.2046, 2021.

Eldering, A., Taylor, T. E., O'Dell, C. W., and Pavlick, R.: The OCO-3 mission: measurement objectives and expected performance based on
1 year of simulated data, Atmospheric Measurement Techniques, 12, 2341–2370, 2019.

Famulari, D., Nemitz, E., Di Marco, C., Phillips, G. J., Thomas, R., House, E., and Fowler, D.: Eddy-covariance measurements of nitrous
oxide fluxes above a city, Agricultural and forest meteorology, 150, 786–793, 2010.

Fasoli, B., Lin, J. C., Bowling, D. R., Mitchell, L., and Mendoza, D.: Simulating atmospheric tracer concentrations for spatially distributed
receptors: updates to the Stochastic Time-Inverted Lagrangian Transport model's R interface (STILT-R version 2), Geoscientific Model
Development, 11, 2813–2824, 2018.

Fujinawa, T., Kuze, A., Suto, H., Shiomi, K., Kanaya, Y., Kawashima, T., Kataoka, F., Mori, S., Eskes, H., and Tanimoto, H.: First concurrent
observations of NO2 and CO2 from power plant plumes by airborne remote sensing, Geophysical Research Letters, 48, e2021GL092 685,
2021.

Ghasemifard, H., Vogel, F. R., Yuan, Y., Luepke, M., Chen, J., Ries, L., Leuchner, M., Schunk, C., Noreen Vardag, S., and Menzel, A.:
Pollution events at the high-altitude mountain site Zugspitze-Schneefernerhaus (2670 m asl), Germany, Atmosphere, 10, 330, 2019.

Gurney, K. R., Patarasuk, R., Liang, J., Song, Y., O'Keeffe, D., Rao, P., Whetstone, J. R., Duren, R. M., Eldering, A., and Miller, C.: The
Hestia fossil fuel CO_2 emissions data product for the Los Angeles megacity (Hestia-LA), Earth System Science Data, 11, 1309–1335,
https://doi.org/10.5194/essd-11-1309-2019, 2019.

Hakkarainen, J., Szelag, M. E., Ialongo, I., Retscher, C., Oda, T., and Crisp, D.: Analyzing nitrogen oxides to carbon dioxide
emission ratios from space: A case study of Matimba Power Station in South Africa, Atmospheric Environment: X, p. 100110,
https://doi.org/10.1016/j.aeaoa.2021.100110, 2021.

Han, S., Kondo, Y., Oshima, N., Takegawa, N., Miyazaki, Y., Hu, M., Lin, P., Deng, Z., Zhao, Y., Sugimoto, N., et al.: Temporal variations
of elemental carbon in Beijing, Journal of Geophysical Research: Atmospheres, 114, 2009.

Harrison, R. M., Dall'Osto, M., Beddows, D., Thorpe, A. J., Bloss, W. J., Allan, J. D., Coe, H., Dorsey, J. R., Gallagher, M., Martin, C., et al.:
Atmospheric chemistry and physics in the atmosphere of a developed megacity (London): an overview of the REPARTEE experiment and
its conclusions, Atmospheric Chemistry and Physics, 12, 3065–3114, 2012.

Haszpra, L., Ferenczi, Z., and Barcza, Z.: Estimation of greenhouse gas emission factors based on observed covariance of CO_2 , CH_4 , N2O
and CO mole fractions, Environmental Sciences Europe, 31, https://doi.org/10.1186/s12302-019-0277-y, 2019.

Hedelius, J. K., Viatte, C., Wunch, D., Roehl, C. M., Toon, G. C., Chen, J., Jones, T., Wofsy, S. C., Franklin, J. E., Parker, H., Dubey, M. K.,
and Wennberg, P. O.: Assessment of errors and biases in retrievals of XCO_2 , XCH_4 , XCO, and XN2O from a 0.5 cm-1 resolution
solar-viewing spectrometer, Atmospheric Measurement Techniques, 9, 3527–3546, https://doi.org/10.5194/amt-9-3527-2016, 2016.

Hedelius, J. K., Liu, J., Oda, T., Maksyutov, S., Roehl, C. M., Iraci, L. T., Podolske, J. R., Hillyard, P. W., Liang, J., Gurney, K. R., Wunch, D., and Wennberg, P. O.: Southern California megacity CO_2, CH_4, and CO flux estimates using ground-and space-based remote sensing and a Lagrangian model, Atmospheric Chemistry and Physics, 18, 16 271–16 291, https://doi.org/10.5194/acp-18-16271-2018, 2018.

650   Huang, X., Wang, T., Talbot, R., Xie, M., Mao, H., Li, S., Zhuang, B., Yang, X., Fu, C., Zhu, J., et al.: Temporal characteristics of atmospheric CO2 in urban Nanjing, China, Atmospheric Research, 153, 437–450, 2015.

Kaiser, J., Heil, A., Andreae, M., Benedetti, A., Chubarova, N., Jones, L., Morcrette, J.-J., Razinger, M., Schultz, M., Suttie, M., et al.: Biomass burning emissions estimated with a global fire assimilation system based on observed fire radiative power, Biogeosciences, 9, 527–554, 2012.

655   Kerr, G. H., Goldberg, D. L., and Anenberg, S. C.: COVID-19 pandemic reveals persistent disparities in nitrogen dioxide pollution, Proceedings of the National Academy of Sciences, 118, 2021.

Kiel, M., Eldering, A., Roten, D. D., Lin, J. C., Feng, S., Lei, R., Lauvaux, T., Oda, T., Roehl, C. M., Blavier, J.-F., et al.: Urban-focused satellite CO2 observations from the Orbiting Carbon Observatory-3: A first look at the Los Angeles megacity, Remote Sensing of Environment, 258, 112 314, 2021.

660   Lai, S., Baker, A., Schuck, T., Velthoven, P. v., Oram, D., Zahn, A., Hermann, M., Weigelt, A., Slemr, F., Brenninkmeijer, C., et al.: Pollution events observed during CARIBIC flights in the upper troposphere between South China and the Philippines, Atmospheric Chemistry and Physics, 10, 1649–1660, 2010.

Lama, S., Houweling, S., Boersma, K. F., Eskes, H., Aben, I., Gon, H. A. C. D. V. D., Krol, M. C., Dolman, H., Borsdorff, T., and Lorente, A.: Quantifying burning efficiency in megacities using the NO_2:CO ratio from the Tropospheric Monitoring Instrument (TROPOMI), 665   Atmospheric Chemistry and Physics, 20, 10 295–10 310, https://doi.org/10.5194/acp-20-10295-2020, 2020.

Laughner, J. L., Neu, J. L., Schimel, D., Wennberg, P. O., Barsanti, K., Bowman, K. W., Chatterjee, A., Croes, B. E., Fitzmaurice, H. L., Henze, D. K., et al.: Societal shifts due to COVID-19 reveal large-scale complexities and feedbacks between atmospheric chemistry and climate change, Proceedings of the National Academy of Sciences, 118, 2021.

Lei, R., Feng, S., Danjou, A., Broquet, G., Wu, D., Lin, J. C., O'Dell, C. W., and Lauvaux, T.: Fossil fuel CO2 emissions over metropolitan 670   areas from space: A multi-model analysis of OCO-2 data over Lahore, Pakistan, Remote Sensing of Environment, 264, 112 625, 2021.

Lin, J. and Gerbig, C.: Accounting for the effect of transport errors on tracer inversions, Geophysical Research Letters, 32, 2005.

Lin, J., Gerbig, C., Wofsy, S., Andrews, A., Daube, B., Davis, K., and Grainger, C.: A near-field tool for simulating the upstream influence of atmospheric observations: The Stochastic Time-Inverted Lagrangian Transport (STILT) model, Journal of Geophysical Research: Atmospheres, 108, 2003.

675   Lin, J. C., Mitchell, L., Crosman, E., Mendoza, D. L., Buchert, M., Bares, R., Fasoli, B., Bowling, D. R., Pataki, D., Catharine, D., Strong, C., Gurney, K. R., Patarasuk, R., Baasandorj, M., Jacques, A., Hoch, S., Horel, J., and Ehleringer, J.: CO2 and carbon emissions from cities linkages to air quality, socioeconomic activity, and stakeholders in the Salt Lake city urban area, Bulletin of the American Meteorological Society, 99, 2325–2339, https://doi.org/10.1175/BAMS-D-17-0037.1, 2018.

Lin, J. C., Bares, R., Fasoli, B., Garcia, M., Crosman, E., and Lyman, S.: Declining methane emissions and steady, high leakage rates observed 680   over multiple years in a western US oil/gas production basin, Scientific reports, 11, 1–12, 2021.

Lindenmaier, R., Dubey, M. K., Henderson, B. G., Butterfield, Z. T., Herman, J. R., Rahn, T., and Lee, S. H.: Multiscale observations of CO_2, $^{13}CO_2$, and pollutants at Four Corners for emission verification and attribution, Proceedings of the National Academy of Sciences of the United States of America, 111, 8386–8391, https://doi.org/10.1073/pnas.1321883111, 2014.

Lopez, M., Schmidt, M., Delmotte, M., Colomb, A., Gros, V., Janssen, C., Lehman, S. J., Mondelain, D., Perrussel, O., Ramonet, M., Xueref-
Remy, I., and Bousquet, P.: CO, NOx and 13CO$_2$ as tracers for fossil fuel CO$_2$: Results from a pilot study in Paris during winter 2010,
Atmospheric Chemistry and Physics, 13, 7343–7358, https://doi.org/10.5194/acp-13-7343-2013, 2013.

Makarova, M. V., Alberti, C., Ionov, D. V., Hase, F., Foka, S. C., Blumenstock, T., Warneke, T., Virolainen, Y. A., Kostsov, V. S., Frey, M.,
Poberovskii, A. V., Timofeyev, Y. M., Paramonova, N. N., Volkova, K. A., Zaitsev, N. A., Biryukov, E. Y., Osipov, S. I., Makarov,
B. K., Polyakov, A. V., Ivakhov, V. M., Imhasin, H. K., and Mikhailov, E. F.: Emission Monitoring Mobile Experiment (EMME):
An overview and first results of the St. Petersburg megacity campaign 2019, Atmospheric Measurement Techniques, 14, 1047–1073,
https://doi.org/10.5194/amt-14-1047-2021, 2021.

Miller, S. M., Matross, D. M., Andrews, A. E., Millet, D. B., Longo, M., Gottlieb, E. W., Hirsch, A. I., Gerbig, C., Lin, J. C., Daube, B. C.,
et al.: Sources of carbon monoxide and formaldehyde in North America determined from high-resolution atmospheric data, Atmospheric
Chemistry and Physics, 8, 7673–7696, 2008.

Mitchell, L. E., Lin, J. C., Bowling, D. R., Pataki, D. E., Strong, C., Schauer, A. J., Bares, R., Bush, S. E., Stephens, B. B., Mendoza, D.,
et al.: Long-term urban carbon dioxide observations reveal spatial and temporal dynamics related to urban characteristics and growth,
Proceedings of the National Academy of Sciences, 115, 2912–2917, 2018.

Moldanová, J., Fridell, E., Popovicheva, O., Demirdjian, B., Tishkova, V., Faccinetto, A., and Focsa, C.: Characterisation of particulate matter
and gaseous emissions from a large ship diesel engine, Atmospheric Environment, 43, 2632–2641, 2009.

Nathan, B., Lauvaux, T., Turnbull, J., and Gurney, K.: Investigations into the use of multi-species measurements for source apportionment of
the Indianapolis fossil fuel CO$_2$ signal, Elementa, 6, https://doi.org/10.1525/elementa.131, 2018.

O'Shea, S. J., Allen, G., Fleming, Z. L., Bauguitte, S. J.-B., Percival, C. J., Gallagher, M. W., Lee, J., Helfter, C., and Nemitz, E.: Area fluxes
of carbon dioxide, methane, and carbon monoxide derived from airborne measurements around Greater London: A case study during
summer 2012, Journal of Geophysical Research: Atmospheres, 119, 4940–4952, 2014.

Palmer, P. I., Suntharalingam, P., Jones, D. B., Jacob, D. J., Streets, D. G., Fu, Q., Vay, S. A., and Sachse, G. W.: Using CO$_2$: CO correlations
to improve inverse analyses of carbon fluxes, Journal of Geophysical Research Atmospheres, 111, https://doi.org/10.1029/2005JD006697,
2006.

Park, H., Jeong, S., Park, H., Labzovskii, L. D., and Bowman, K. W.: An assessment of emission characteristics of Northern Hemisphere cities
using spaceborne observations of CO$_2$, CO, and NO$_2$, Remote Sensing of Environment, 254, https://doi.org/10.1016/j.rse.2020.112246,
2021.

Pitt, J. R., Allen, G., Bauguitte, S. J.-B., Gallagher, M. W., Lee, J. D., Drysdale, W., Nelson, B., Manning, A. J., and Palmer, P. I.: Assessing
London CO2, CH4 and CO emissions using aircraft measurements and dispersion modelling, Atmospheric Chemistry and Physics, 19,
8931–8945, 2019.

Plant, G., Kort, E. A., Floerchinger, C., Gvakharia, A., Vimont, I., and Sweeney, C.: Large fugitive methane emissions from urban centers
along the US East Coast, Geophysical research letters, 46, 8500–8507, 2019.

Popa, M. E., Vollmer, M. K., Jordan, A., Brand, W. A., Pathirana, S. L., Rothe, M., and Röckmann, T.: Vehicle emissions of greenhouse
gases and related tracers from a tunnel study: CO : CO$_2$, N2O : CH$_4$: O2 : Atios, and the stable isotopes 13C and 18O in CO$_2$ and CO,
Atmospheric Chemistry and Physics, 14, 2105–2123, https://doi.org/10.5194/acp-14-2105-2014, 2014.

Reuter, M., Buchwitz, M., Schneising, O., Krautwurst, S., O'Dell, C. W., Richter, A., Bovensmann, H., and Burrows, J. P.: Towards moni-
toring localized CO$_2$ emissions from space: Co-located regional CO$_2$ and NO$_2$ enhancements observed by the OCO-2 and S5P satellites,
Atmospheric Chemistry and Physics, 19, 9371–9383, https://doi.org/10.5194/acp-19-9371-2019, 2019.

Russo, R., Talbot, R., Dibb, J. E., Scheuer, E., Seid, G., Jordan, C., Fuelberg, H., Sachse, G., Avery, M., Vay, S., et al.: Chemical composition of Asian continental outflow over the western Pacific: Results from Transport and Chemical Evolution over the Pacific (TRACE-P), Journal of Geophysical Research: Atmospheres, 108, 2003.

725 Schuh, A. E., Otte, M., Lauvaux, T., and Oda, T.: Far-field biogenic and anthropogenic emissions as a dominant source of variability in local urban carbon budgets: A global high-resolution model study with implications for satellite remote sensing, Remote Sensing of Environment, 262, 112 473, 2021.

Shekhar, A., Chen, J., Paetzold, J. C., Dietrich, F., Zhao, X., Bhattacharjee, S., Ruisinger, V., and Wofsy, S. C.: Anthropogenic $CO2$ emissions assessment of Nile Delta using XCO2 and SIF data from OCO-2 satellite, Environmental Research Letters, 15, 095 010, 2020.

730 Silva, S. and Arellano, A.: Characterizing Regional-Scale Combustion Using Satellite Retrievals of CO, NO_2 and CO_2 , Remote Sensing, 9, 744, https://doi.org/10.3390/rs9070744, 2017.

Silva, S. J., Arellano, A. F., and Worden, H. M.: Toward anthropogenic combustion emission constraints from space-based analysis of urban CO_2 /CO sensitivity, Geophysical Research Letters, 40, 4971–4976, https://doi.org/10.1002/grl.50954, 2013.

Sim, S., Jeong, S., Park, H., Park, C., Kwak, K. H., Lee, S. B., Kim, C. H., Lee, S., Chang, J. S., Kang, H., and Woo, J. H.: Co-benefit
735 potential of urban CO_2 and air quality monitoring: A study on the first mobile campaign and building monitoring experiments in Seoul during the winter, Atmospheric Pollution Research, 11, 1963–1970, https://doi.org/10.1016/j.apr.2020.08.009, 2020.

Solazzo, E., Crippa, M., Guizzardi, D., Muntean, M., Choulga, M., and Janssens-Maenhout, G.: Uncertainties in the Emissions Database for Global Atmospheric Research (EDGAR) emission inventory of greenhouse gases, Atmospheric Chemistry and Physics, 21, 5655–5683, https://doi.org/10.5194/acp-21-5655-2021, 2021.

740 Stewart, I. D. and Oke, T. R.: Local climate zones for urban temperature studies, Bulletin of the American Meteorological Society, 93, 1879–1900, 2012.

Super, I., van der Gon, H. A. D., Visschedijk, A. J., Moerman, M. M., Chen, H., van der Molen, M. K., and Peters, W.: Interpreting continuous in-situ observations of carbon dioxide and carbon monoxide in the urban port area of Rotterdam, Atmospheric Pollution Research, 8, 174–187, https://doi.org/10.1016/j.apr.2016.08.008, 2017.

745 Surl, L., Palmer, P. I., and González Abad, G.: Which processes drive observed variations of HCHO columns over India?, Atmospheric Chemistry and Physics, 18, 4549–4566, 2018.

Tang, W., Arellano, A. F., DiGangi, J. P., Choi, Y., Diskin, G. S., Agustí-Panareda, A., Parrington, M., Massart, S., Gaubert, B., Lee, Y., et al.: Evaluating high-resolution forecasts of atmospheric CO and CO 2 from a global prediction system during KORUS-AQ field campaign, Atmospheric Chemistry and Physics, 18, 11 007–11 030, 2018.

750 Tang, W., Gaubert, B., Emmons, L., Choi, Y., DiGangi, J., Diskin, G., Xu, X., He, C., Worden, H., Tilmes, S., Buchholz, R., Halliday, H., and Arellano, A.: On the relationship between tropospheric CO and CO_2 during KORUS-AQ and its role in constraining anthropogenic CO_2 , Atmospheric Chemistry and Physics, pp. 1–53, https://doi.org/10.5194/acp-2020-864, 2020.

Taylor, T. E., Eldering, A., Merrelli, A., Kiel, M., Somkuti, P., Cheng, C., Rosenberg, R., Fisher, B., Crisp, D., Basilio, R., et al.: OCO-3 early mission operations and initial (vEarly) XCO2 and SIF retrievals, Remote Sensing of Environment, 251, 112 032, 2020.

755 Turnbull, J., Karion, A., Fischer, M., Faloona, I., Guilderson, T., Lehman, S., Miller, B., Miller, J., Montzka, S., Sherwood, T., et al.: Assessment of fossil fuel carbon dioxide and other anthropogenic trace gas emissions from airborne measurements over Sacramento, California in spring 2009, Atmospheric Chemistry and Physics, 11, 705–721, 2011a.

Atmospheric
Chemistry
and Physics
Discussions

Turnbull, J. C., Tans, P. P., Lehman, S. J., Baker, D., Conway, T. J., Chung, Y. S., Gregg, J., Miller, J. B., Southon, J. R., and Zhou, L. X.: Atmospheric observations of carbon monoxide and fossil fuel CO_2 emissions from East Asia, Journal of Geophysical Research Atmospheres, 116, https://doi.org/10.1029/2011JD016691, 2011b.

Turnbull, J. C., Sweeney, C., Karion, A., Newberger, T., Lehman, S. J., Tans, P. P., Davis, K. J., Lauvaux, T., Miles, N. L., Richardson, S. J., et al.: Toward quantification and source sector identification of fossil fuel CO2 emissions from an urban area: Results from the INFLUX experiment, Journal of Geophysical Research: Atmospheres, 120, 292–312, 2015.

Turner, A. J., Köhler, P., Magney, T. S., Frankenberg, C., Fung, I., and Cohen, R. C.: A double peak in the seasonality of California's photosynthesis as observed from space, Biogeosciences, 17, 405–422, 2020.

Veefkind, J., Aben, I., McMullan, K., Förster, H., De Vries, J., Otter, G., Claas, J., Eskes, H., De Haan, J., Kleipool, Q., et al.: TROPOMI on the ESA Sentinel-5 Precursor: A GMES mission for global observations of the atmospheric composition for climate, air quality and ozone layer applications, Remote sensing of environment, 120, 70–83, 2012.

Venables, W. N. and Ripley, B. D.: Modern Applied Statistics with S, Springer, New York, fourth edn., http://www.stats.ox.ac.uk/pub/MASS4, iSBN 0-387-95457-0, 2002.

Vollmer, M. K., Juergens, N., Steinbacher, M., Reimann, S., Weilenmann, M., and Buchmann, B.: Road vehicle emissions of molecular hydrogen (H2) from a tunnel study, Atmospheric Environment, 41, 8355–8369, 2007.

Wang, H., Jacob, D. J., Kopacz, M., Jones, D. B. A., Suntharalingam, P., Fisher, J. A., Nassar, R., Pawson, S., and Nielsen, J. E.: Atmospheric Chemistry and Physics Error correlation between CO_2 and CO as constraint for CO_2 flux inversions using satellite data, Atmos. Chem. Phys, 9, 7313–7323, www.atmos-chem-phys.net/9/7313/2009/, 2009.

Wang, X., Lei, Y., Yan, L., Liu, T., Zhang, Q., and He, K.: A unit-based emission inventory of SO2, NOx and PM for the Chinese iron and steel industry from 2010 to 2015, Science of the total environment, 676, 18–30, 2019.

Wang, Y., Munger, J. W., Xu, S., McElroy, M. B., Hao, J., Nielsen, C. P., and Ma, H.: CO_2 and its correlation with CO at a rural site near Beijing: Implications for combustion efficiency in China, Atmospheric Chemistry and Physics, 10, 8881–8897, https://doi.org/10.5194/acp-10-8881-2010, 2010.

Wennberg, P. O., Mui, W., Wunch, D., Kort, E. A., Blake, D. R., Atlas, E. L., Santoni, G. W., Wofsy, S. C., Diskin, G. S., Jeong, S., et al.: On the sources of methane to the Los Angeles atmosphere, Environmental science & technology, 46, 9282–9289, 2012.

Westerdahl, D., Wang, X., Pan, X., and Zhang, K. M.: Characterization of on-road vehicle emission factors and microenvironmental air quality in Beijing, China, Atmospheric Environment, 43, 697–705, 2009.

Williams, E., Lerner, B., Murphy, P., Herndon, S., and Zahniser, M.: Emissions of NOx, SO2, CO, and HCHO from commercial marine shipping during Texas Air Quality Study (TexAQS) 2006, Journal of Geophysical Research: Atmospheres, 114, 2009.

Wu, D., Lin, J. C., Fasoli, B., Oda, T., Ye, X., Lauvaux, T., Yang, E. G., and Kort, E. A.: A Lagrangian approach towards extracting signals of urban CO 2 emissions from satellite observations of atmospheric column CO 2 (XCO 2): X-Stochastic Time-Inverted Lagrangian Transport model ("X-STILT v1"), Geoscientific Model Development, 11, 4843–4871, 2018.

Wu, D., Lin, J. C., Oda, T., and Kort, E. A.: Space-based quantification of per capita CO2 emissions from cities, Environmental Research Letters, 15, 035 004, 2020.

Wu, D., Lin, J. C., Duarte, H. F., Yadav, V., Parazoo, N. C., Oda, T., and Kort, E. A.: A model for urban biogenic CO 2 fluxes: Solar-Induced Fluorescence for Modeling Urban biogenic Fluxes (SMUrF v1), Geoscientific Model Development, 14, 3633–3661, 2021.

Wunch, D., Wennberg, P., Toon, G., Keppel-Aleks, G., and Yavin, Y.: Emissions of greenhouse gases from a North American megacity, Geophysical research letters, 36, 2009.

Xia, L., Zhang, G., Liu, L., Li, B., Zhan, M., Kong, P., and Wang, H.: Atmospheric CO2 and CO at Jingdezhen station in central China: Understanding the regional transport and combustion efficiency, Atmospheric Environment, 222, 117 104, 2020.

Ye, X., Lauvaux, T., Kort, E. A., Oda, T., Feng, S., Lin, J. C., Yang, E. G., and Wu, D.: Constraining Fossil Fuel CO2 Emissions From Urban Area Using OCO-2 Observations of Total Column CO2, Journal of Geophysical Research: Atmospheres, 125, e2019JD030 528, 2020.

800 Yokota, T., Yoshida, Y., Eguchi, N., Ota, Y., Tanaka, T., Watanabe, H., and Maksyutov, S.: Global concentrations of CO2 and CH4 retrieved from GOSAT: First preliminary results, Sola, 5, 160–163, 2009.

Yuan, L. and Smith, A. C.: CO and CO2 emissions from spontaneous heating of coal under different ventilation rates, International Journal of Coal Geology, 88, 24–30, 2011.

Zhang, F., Chen, Y., Tian, C., Lou, D., Li, J., Zhang, G., and Matthias, V.: Emission factors for gaseous and particulate pollutants from

805 offshore diesel engine vessels in China, Atmospheric Chemistry and Physics, 16, 6319–6334, 2016.

Zhang, Y., Joiner, J., Alemohammad, S. H., Zhou, S., and Gentine, P.: A global spatially contiguous solar-induced fluorescence (CSIF) dataset using neural networks, Biogeosciences, 15, 5779–5800, 2018.